System performance of a prototype flat-panel imager operated under mammographic conditions

Kyung-Wook Jee,[a] Larry E. Antonuk, Youcef El-Mohri, and Qihua Zhao
Department of Radiation Oncology, University of Michigan Medical Center, Ann Arbor, Michigan 48109

The results of an empirical and theoretical investigation of the performance of a high-resolution, active matrix flat-panel imager performed under mammographic conditions are reported. The imager is based upon a prototype, indirect detection active matrix array incorporating a discrete photodiode in each pixel and a pixel-to-pixel pitch of 97 μm. The investigation involved three imager configurations corresponding to the use of three different x-ray converters with the array. The converters were a conventional Gd_2O_2S-based mammographic phosphor screen (Min-R) and two structured CsI:Tl scintillators: one optimized for high spatial resolution (FOS-HR) and the other for high light output (FOS-HL). Detective quantum efficiency for mammographic exposures ranging from ~ 2 to ~ 40 mR at 26 kVp were determined for each imager configuration through measurements of x-ray sensitivity, modulation transfer function (MTF), and noise power spectrum (NPS). All configurations were found to provide significant presampling MTF at frequencies beyond the Nyquist frequency of the array, ~ 5.2 mm^{-1}, consistent with the high spatial resolution of the converters. In addition, the effect of additive electronic noise on the NPS was found to be significantly larger for the configuration with lower system gain (FOS-HR) than for the configurations with higher gain (Min-R, FOS-HL). The maximum DQE values obtained with the CsI:Tl scintillators were considerably greater than those obtained with the Min-R screen due to the significantly lower Swank noise of the scintillators. Moreover, DQE performance was found to degrade with decreasing exposure, although this exposure-dependence was considerably reduced for the higher gain configurations. Theoretical calculations based on the cascaded systems model were found to be in generally good agreement with these empirically determined NPS and DQE values. In this study, we provide an example of how cascaded systems modeling can be used to identify factors limiting system performance and to examine trade-offs between factors toward the goal of maximizing performance. © *2003 American Association of Physicists in Medicine.*
[DOI: 10.1118/1.1585051]

I. INTRODUCTION

In recent years, the rapid development of active matrix flat-panel technology has resulted in the introduction of versatile, digital x-ray imagers for a variety of x-ray applications. These applications include radiography, fluoroscopy, cone-beam CT, radiotherapy portal imaging, relative dosimetry, and mammography. For a given imaging application, it is highly useful to assess the system performance of flat-panel technology under conditions relevant to the application. Such objective performance assessments can facilitate quantitative comparisons both with other existing technologies as well as with theoretical expectations based on detailed mathematical models. Furthermore, such comparisons can be used to identify problems or weaknesses in the technology toward the goal of achieving maximum theoretical performance.

In this context, the measurement and evaluation of observer-independent performance variables (OIPVs) such as modulation transfer function (MTF), noise power spectrum (NPS), and detective quantum efficiency (DQE) provide a valid, objective means of characterizing imaging system performance in the spatial frequency domain.[1–3] These performance variables quantitatively describe the signal and noise transfer properties of an imaging system from the input end to the output end of the system. An imaging system which efficiently transfers the signal-to-noise information of incident x-ray quanta to the end of the system has high DQE and is therefore considered to exhibit high performance.[3]

Recently, there have been extensive efforts to develop and critically evaluate large area, high-resolution flat-panel imagers (FPIs) for digital mammographic applications. For example, an indirect detection mammographic imager, based on a 100 μm pixel-to-pixel pitch, flat-panel array with discrete photodiodes and a structured CsI:Tl scintillator, has been commercially introduced and its frequency-dependent DQE performance has been reported for various mammographic exposures.[4] In addition, the DQE performance of direct detection imagers employing a-Se photoconductors (an 85 μm pitch imager design with an ~ 200 μm thick a-Se converter,[5] and a 70 μm pitch design with an ~ 250 μm thick a-Se converter[6]) has been also reported. Generally, initial results from these imagers suggest that, over the frequency range provided by the imagers, DQE performance

comparable or superior to that of mammographic screen-film systems is possible.

In the present paper, we report a quantitative evaluation of three configurations of a prototype indirect-detection, flat-panel imager operated under various mammographic conditions. Each configuration involves a 97 μm pitch array that detects the radiation by means of one of three overlying x-ray converters. Empirical measurements of the x-ray sensitivity, MTF, and NPS were performed to determine the DQE performance of these three configurations. In addition, using the cascaded systems formalism,[7–9] the DQE performance was theoretically modeled and the resulting DQE calculations are compared to the corresponding measurements.

II. METHODS AND MATERIALS

A. Description of active matrix flat-panel imager (AMFPI) configurations

Each configuration of the AMFPI used in these studies consists of three sub-systems: a two-dimensional pixelated imaging array, an x-ray converter, and an electronic acquisition system. Each of these sub-systems is described below.

1. Flat-panel array

The array used in these studies has a pixel format of 2048×2048 and a pixel-to-pixel pitch of 97 μm, giving an active area of ~19.9×19.9 cm^2. This array (designated "Hawkeye") was specifically designed to explore the use of active matrix, flat-panel imaging technology for high-resolution radiographic applications as well as for variable resolution fluoroscopic imaging.[10] The general structure and operation of this array are similar to that of earlier indirect-detection arrays developed by our group and others.[11,12] Design specifications and operational characteristics of the array are summarized in Table I. Each array pixel comprises a single amorphous silicon (a-Si:H) thin-film transistor (TFT) coupled to a discrete a-Si:H n-i-p photodiode. In this design, a relatively large fraction of the pixel area is insensitive to incident light photons due to the array fabrication requirement that the photodiode overlaps neither the pixel addressing lines nor the pixel TFT. Consequently, for this relatively high-resolution design, the optical fill factor (defined as the fraction of the pixel area that is sensitive to optical illumination) is only ~45%.

While only a single array of this design was available for these studies, the level of performance from this array was consistent with that of high quality arrays of similar designs. For example, while the absolute magnitude of the dark signal from the pixel cannot be determined due to the contribution of an unknown offset charge from the acquisition electronics, the dark current of the pixel can be determined through a measurement of the relative dark pixel signal as a function of frame time (T_{FRAME}).[12] (Frame time is defined as the interval that the pixel TFTs are kept nonconducting in order to allow signal to accumulate in the capacitance of the photodiode between the readout of consecutive image frames.)

TABLE I. Design specifications and operational characteristics of the flat-panel array used in these studies. All pixel properties correspond to operation of the array at a photodiode reversed bias voltage (V_{BIAS}) of -6 V. The value listed for the maximum frame rate corresponds to the assumption that the pixel TFTs are kept conducting for five times longer than the pixel time constant, τ_{RC}. The maximum frame time corresponds to the interval that the array pixels can be kept nonconductive before the signal-storage capacity becomes saturated by the pixel dark signal. The ranges of linearity reported correspond to the maximum pixel signal size for which deviation from a linear signal response is less than ~1%. In addition, the value given for the intrinsic pixel noise corresponds to a calculation of the TFT thermal noise, $\sqrt{2kTC_{\text{PD}}}$, where k is the Boltzmann constant, T is the absolute temperature in Kelvin, and C_{PD} is the capacitance of the pixel photodiode. The TFTs were operated at voltages of 6 V and -8 V to render them conducting and nonconducting, respectively.

|	
Pixel format (data×gate)	2048×2048
Pixel pitch	97 μm
Array dimension	19.9×19.9 cm^2
Data line capacitance	~50 pF
TFT dimensions ($L×W$)	9.5×12 μm^2
Photodiode geometric area	~69×76 μm^2
Optical fill factor	~45%
Photodiode capacitance, C_{PD}	~0.34 pF
Pixel signal capacity ($=C_{\text{PD}}×V_{\text{BIAS}}$)	~2.0 pC
Maximum frame rate	~40 fps
Pixel dark current	~0.81 fA
Maximum frame time	⩾30 s
Range of linearity (radiographic)	up to ~60% of pixel saturation
(fluoroscopic)	up to ~40% of pixel saturation
Charge trapping	~10 to ~23%
Dark signal drift	Negligible
Intrinsic pixel noise	~340 e (rms)
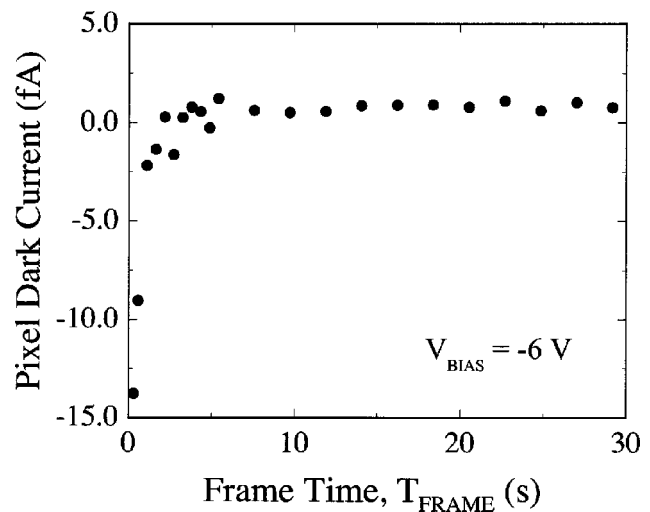
FIG. 1. A plot of the pixel dark current as a function of frame time, T_{FRAME}. The data are derived from the measurement of the pixel dark signal using the technique outlined in Ref. 12. These data (and those shown throughout the paper) were acquired at a photodiode bias voltage, V_{BIAS}, of -6 V. In addition, these data (and those shown for Fig. 2) are from a single pixel whose performance is representative of correctly functioning pixels in the array. The change of polarity observed in the data at a frame time of ~3 s is due to the contribution of the TFT transient current, which is opposite in polarity to the photodiode current and decreases exponentially with increasing frame time. (See Refs. 12 and 55 for a detailed description.)

(a)

Light Signal (#LED flashes)
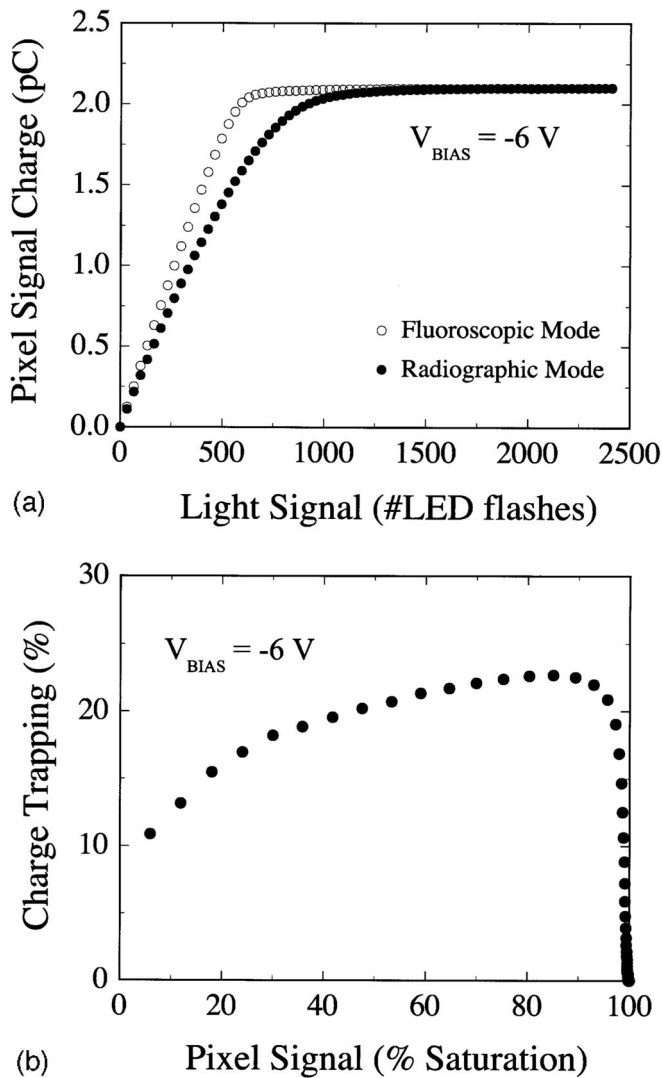

(b)

Pixel Signal (% Saturation)

FIG. 2. (a) A plot of the signal response of a pixel to incident light signal, in units of the number of LED flashes. (The LED used in this measurement has a peak emission wavelength of approximately 570 nm.) Data are presented for both fluoroscopic and radiographic modes of operation. For each data point, the corresponding dark signal has been subtracted. (b) A plot of the trapped charge as a function of the fluoroscopic pixel signal size, in units of percentage saturation of the pixel. These charge trapping values were obtained from the data in Fig. 2(a) using the technique described in Ref. 12.

Measurements of the pixel dark current for the Hawkeye array, which are shown in Fig. 1, demonstrate a behavior seen in earlier array designs. As a function of frame time, dark current changes rapidly from -13.8 fA at $T_{\mathrm{FRAME}}=29$ ms to 0.3 fA at 2.2 s and thereafter changes much more slowly, reaching a value of ~1.0 fA at 22 s. Throughout, the magnitude of the dark signal is very low, thereby allowing frame times in excess of ~30 s without saturating the signal-storage capacity of the pixels. Moreover, the pixels exhibit negligible variation in relative dark signal over time (not shown)—with less than 1% change over an 8-hour period.

Measurements of the pixel signal response as a function of incident illumination are shown in Fig. 2(a). Data are shown for both fluoroscopic and radiographic modes of operation. (The description and timing diagram of each of these

operational modes are detailed in Ref. 12.) The pixel response is highly linear, with deviations from linearity of less than 1% for pixel signals up to $\sim60\%$ (40%) of saturation for a fluoroscopic (radiographic) mode. In radiographic mode, the signal response is lower due to the trapping of charge in metastable states in the a-Si:H photodiodes.[12] As the incident light signal increases, the response deviates increasingly from linearity until the pixel becomes saturated. The fluoroscopic and radiographic responses merge at saturation. From the saturation level of this pixel response, the capacitance of the pixel, C_{PD}, can be deduced from

$$C_{\mathrm{PD}}=\frac{Q_{\mathrm{SAT}}}{V_{\mathrm{BIAS}}}, \tag{1}$$

where Q_{SAT} represents the amount of pixel signal at saturation.[12] From the measured saturation level, the value of C_{PD} was deduced to be ~0.34 pF, which is in good agreement with a calculated value of ~0.33 pF based on the design of the array. In Fig. 2(b), the trapped charge (expressed as a percent of the corresponding fluoroscopic signal) is plotted as a function of pixel signal size (expressed as a percent of the pixel saturation level). As the pixel signal increases, the trapped charge increases from a low of $\sim10\%$ up to $\sim23\%$. The general behavior of the linearity and charge trapping for this array is similar to that observed from earlier arrays.[12,14] Moreover, the range of highly linear behavior and degree of charge trapping is consistent with good array quality.

2. X-ray converters

The Hawkeye array detects x rays by means of an x-ray converter in the form of an overlying scintillator. Three types of scintillators, whose physical properties are suitable for mammographic imaging, were employed in this study. One scintillator was a Gd_2O_2S:Tb phosphor screen with a surface density of ~34 mg/cm^2 (Min-R, Eastman Kodak). The other two scintillators each consisted of 150 μm thick, structured CsI:Tl grown on a 3 mm thick fiber optic plate (FOS, Hamamatsu): one optimized for high spatial resolution (FOS-HR) and the other for high light output (FOS-HL).[15] The fiber optic plate is a collection of glass capillaries with each capillary having a diameter of ~3–6 μm and a length of ~3 mm. This plate serves as a substrate for the CsI:Tl deposition as well as a light guide by virtue of optical reflection at the boundary of capillaries.

In general, the upper limit of DQE performance for an AMFPI system is primarily determined by two physical properties of its x-ray converter: the x-ray quantum detection efficiency, $\bar{g}_1$, and the Swank factor, I (i.e., $\mathrm{DQE}\leq\bar{g}_1\times I$).[8] For example, for a 26 kVp mammographic beam [with a Molybdenum (Mo) target and a 30 μm Mo filter further hardened by 4 cm of breast tissue (50% glandular and 50% adipose tissue)], the x-ray detection efficiency is calculated to be very high $-\sim75\%$ and $\sim86\%$ for the Min-R and FOS scintillators, respectively. The Swank factor (derived using a technique described in Sec. II C 3) is estimated to be relatively moderate (~0.63 for the Min-R scintillator) or very

high ($\sim$0.98 for the FOS scintillators). This is due to the fact that, at this low beam energy, the process of generation and reabsorption of k-fluorescence x rays is largely absent, and therefore does not significantly contribute to the Swank noise. As a consequence of such favorable properties, these scintillators provide very high DQE and furthermore have the potential to provide high DQE performance when used with the Hawkeye array and low noise acquisition electronics. Moreover, a large DQE at high spatial frequencies is anticipated due to the incorporation of high-resolution scintillators such as the Min-R and FOS-HR converters. The effects of system gain upon DQE performance were quantified through investigations involving the FOS-HR and FOS-HL scintillators whose physical properties are almost identical, other than for scintillator gain and MTF.

3. Electronic acquisition system

The Hawkeye array was read out by a recently developed electronic acquisition system (named G3).[16] The G3 system provides asynchronous operation wherein the direct control of all timing parameters and data flow is executed by complex digital logic circuitry, independent of the host computer. The G3 system offers the ability to address all 2048 $\times$2048 pixels of the array. In general, it is highly desirable that the dark noise be as low as possible so as to allow the total noise of the imaging system to be dominated by the noise of the detected incident x-ray quanta to as low an exposure as possible—ideally down to the lowest exposure limit for the application. Toward this end, the G3 system incorporates a fully customized, low noise, 32-channel preamplifier-multiplexor chip.[17] The use of this chip with the Hawkeye array resulted in a dark noise (the noise of the system in the absence of radiation) of $\sim$2000 e, representing an average for the range of frame times used in this study ($\sim$0.5 to $\sim$2 s). This level of noise is relatively low, given the 50 pF capacitance of the array data lines.

B. Experimental methodology

All x-ray measurements were performed using a mammographic source (Senographe DMR, GE Medical Systems). The source was equipped with a manually selectable, dual-track x-ray tube with a target consisting of a Molybdenum (Mo) track and a Rhodium (Rh) track. Intrinsic beam filtration was carried out with a 30 μm thick Mo filter. For all measurements, the x-ray beam was further hardened by a 4 cm thick breast phantom[18] (tissue-equivalent BR12, Nuclear Associates). The detection surface of the flat-panel imager was positioned at a source-to-detector-distance (SDD) of $\sim$65 cm and the phantom was placed $\sim$40 cm in front of the imager. The automatic exposure controls of the unit were overridden and the mAs control of the unit was adjusted to provide the desired exposure. The magnitude of the exposure to the imager was determined using a calibrated ion chamber (Keithley 96035B with a Keithley dosimeter 35050A). The imager was operated in the radiographic mode.[12] In this mode, the array is repeatedly read out in the absence of radiation (forming "dark frames") until an x-ray irradiation is

delivered and a final readout is performed (forming an "image frame"). The irradiation times used in this study ranged from $\sim$0.5 to 2 s. For a given irradiation time, in order to accommodate the duration of the entire exposure, a fixed-length pause in readout was introduced at the beginning of each frame.

1. Empirical x-ray sensitivity

X-ray sensitivity (defined as the mean pixel signal per unit exposure, with units of e/mR/pixel) for the three imager configurations was measured at energies from 24 to 32 kVp with a Mo/Mo (target/filter) combination. For a given imager configuration and kVp, the signal response of the pixels was measured at five different exposures. These exposure levels were chosen so that the signal size was kept below 10% of pixel saturation thereby ensuring a highly linear pixel response. The mean slope obtained from linear fits to the measured signal response as a function of exposure yielded the x-ray sensitivity. The resulting value of x-ray sensitivity for each energy and configuration served as an empirical input in a theoretical determination of the screen conversion efficiency. (See Sec. II C 3.)

2. Empirical MTF

The MTF of an imaging system, obtained from the Fourier transform of the line spread function (LSF), quantifies the spatial resolution characteristics of the system. Measurements of LSF were performed for each imager configuration at a mammographic energy of 26 kVp with a Mo/Mo target/filter combination. Additional beam hardening was not used as it was found to have a negligible effect on the MTF. Line spread function data were obtained using the angled slit technique[19] and the corresponding MTFs were calculated following the procedure described in Ref. 20. The mechanical slit used for the acquisition of LSF data consisted of a pair of $\sim$15 cm$\times$10 cm$\times$0.6 cm tungsten plates, separated by 10 μm thick shims. A 15 cm slit of x rays was presented to the imager by positioning the slit on the surface of the imager and aligning it with the center of the focal spot. For each configuration, 5 radiographic images of the slit were acquired with the slit tilted at a small, fixed angle (less than 1°) relative to the direction of the data lines, so as to allow over-sampling of the slit image. (Measurements along the gate line direction were not performed since earlier studies with similar arrays had indicated that there are no significant differences in MTFs obtained from orthogonal directions.) For each radiographic image, gain and offset corrections were applied to the data in order to compensate for nonuniformities in the response of the pixels.[21] These slit images were then averaged to yield a single image from which the LSF was determined. Under the conditions of the measurements, for example in the case of the FOS-HR configuration, the resulting LSF has a sampling interval of $\sim$12.2 μm, corresponding to a sampling frequency of $\sim$80 mm^{-1}. This sampling frequency is sufficiently high that aliasing effects, which would otherwise be present if a lower sampling frequency (comparable to that of the pixels, $\sim$10.3 mm^{-1})

were used, are avoided. From the resulting oversampled LSF, the ''presampling'' MTF of the system was determined for each imager configuration.

3. Empirical NPS and DQE

One-dimensional, frequency-dependent noise power spectra, NPS(u), were determined for each of the imager configurations under mammographic irradiation conditions. [The symbol NPS(u) corresponds to a central slice through the origin of the two-dimensional noise power spectrum, NPS(u,v), along one primary axis—i.e., NPS(u) $=$ NPS(u,v)$|_{v=0}$. NPS(u) has units of e^2 mm^2 or mm^2.] The methodology used to measure NPS(u) closely follows that described in a previous paper.[8,22] The analysis of the data was performed using the synthesized slit technique[23–25] with the length of the slit oriented parallel to the data line direction. Conceptually, a slit having dimensions of L $\times 1$ pixels is scanned n times along the orthogonal direction (i.e., along the direction of the gate lines) which, in turn, provides a realization of pixel data for the determination of NPS(u). In practice, a single set of ''scanned'' slit data derives from a contiguous block of $L \times n$ pixels from a single image data frame. A slit length of ~ 3 mm (corresponding to L of ~ 30 pixels of the Hawkeye imager) was used. Independent measurements confirmed that this slit length was sufficient to assure convergence of the resulting NPS(u) under all measurement conditions considered. Earlier analyses with active matrix flat-panel imagers[8,26] indicated that one-dimensional NPS results, NPS(u), which were obtained along one of the primary spatial frequency axes using the synthesized slit technique, are consistent with those obtained along the orthogonal direction, NPS(v)—although one or more peaks due to correlated noise pickup from power supplies and other electromagnetic sources are noticeably present in NPS(v). An alternative method of obtaining one-dimensional NPS results would involve the extraction of such information, NPS(u), from measured two-dimensional NPS results, NPS(u,v), along one of the primary axes.[4,27,28] A previous analysis using a 127 μm pitch flat-panel imager[8] has demonstrated that NPS(u) obtained using the synthesized slit technique leads to results which are consistent with those extracted from measured NPS(u,v).

Measurements of NPS consisted of a series of experimental procedures (including image data acquisition, image data processing, and spectral analysis) that are detailed below. Radiographic image data (''flood fields'') were acquired using a large area x-ray field, with a ''medium format'' collimator setting corresponding to a 13$\times$18 cm^2 field. Data were acquired for exposures ranging from ~ 1 to ~ 38 mR per image data frame at 26 kVp with a Mo/Mo target/filter combination. This range was chosen to be considerably below and above the typical mammographic detector exposure range (with a median of ~ 13 mR[29]) in order to allow an examination of the full potential of the technology. An initialization time, ranging from ~ 22 to ~ 36 s, was introduced between the acquisition of consecutive data frames in order to minimize the effects of charge carryover from one data

frame to the next. During this initialization time, the array was continually read out in the absence of radiation. For each exposure level, gain and offset corrections were determined and applied to each image data frame. For each set of conditions, an ensemble of up to 10 flood fields was thereby obtained for NPS analysis. In addition, image data in the absence of x-ray irradiation (''dark fields'') were acquired in a similar manner. A total of six dark fields were acquired and, after the application of offset corrections to this data, the information was used to determine dark NPS values which served as an input to a theoretical model of the system NPS (see Sec. II C 2).

The flood fields and dark fields were further processed as follows: all pixel values were converted to units of electrons (e); portions of the fields corresponding to pixel and line defects were manually cropped; and the small number of remaining faulty or dead pixels were filtered using a 3$\times$3 median filter affecting less than 0.5% of the total number of pixels. For the dark fields, an even smaller number of pixels were filtered (~ 0.01%) since the only pixels that manifest themselves as defective in the absence of x-ray radiation are those with abnormal dark current behavior. The resulting fields constituted the final sets of data used with the synthesized slit technique.

From the resulting set of data generated for each set of conditions, N independent blocks of pixel data ($N = \sim 300$, ~ 540, and ~ 840), each with dimensions of $L \times n$ pixels ($L \times n = 32 \times 232$, 27×159, and 30×160), were selected for the Min-R, FOS-HR, and FOS-HL configurations, respectively. Each data block was then averaged along the L direction and formed an n-point, one-dimensional data realization, giving a total of N realizations. For each realization, a low frequency background trend was removed by means of a linear-fit subtraction and a ''data window'' (i.e., a Hanning window) was employed to suppress spectral leakage. Fourier transformations of the realizations were then obtained and normalized according to the dimensions of the original slit and data window, producing an ensemble of N power spectra. Finally, the average of the ensemble yielded the measured NPS. For the Min-R, FOS-HR, and FOS-HL configurations, the width, n, of the block of pixels ($n = 232$, 159, and 160, respectively) provided sampling intervals of ~ 0.044, ~ 0.065, and ~ 0.064 mm^{-1}, respectively.

In order to obtain an empirical determination of DQE, the resulting noise power spectra were further normalized to the mean signal values, $\bar{d}$, of the flood field data that were used in the generation of these NPS results. From the normalized NPS, NPS$_N$(f), the measured MTF, MTF(f), and the calculated mean fluence, $\bar{q}_0$ (in units of x-ray photons/mm^2), the DQE was empirically determined using the following equation:[4,28,30]

$$\text{DQE}(f) = \frac{\bar{d}^2 \text{MTF}^2(f)}{\bar{q}_0 \text{NPS}(f)} = \frac{\text{MTF}^2(f)}{\bar{q}_0 \text{NPS}_N(f)}. \tag{2}$$
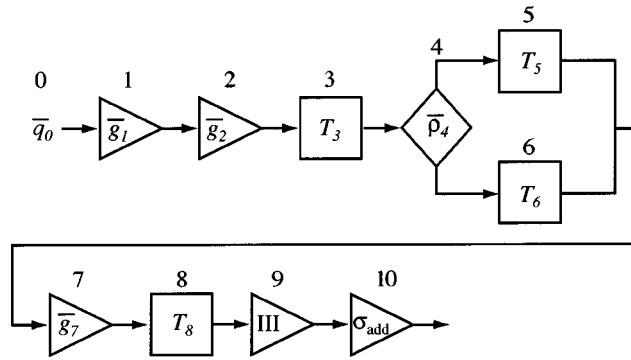
FIG. 3. A block diagram of the cascaded systems model representing the chain of physical processes involved in the formation of x-ray images under mammographic conditions. In this diagram, a number of elementary stages are illustrated in series and in parallel. Each block corresponds to a stage representing either an amplification process or a blurring process. The number printed on top of each block specifies the order of stages in the imaging chain. Stages 1, 2, 4, and 7 represent amplification processes and are also referred to as "gain" stages. Stages 3, 5, 6, and 8 represent blurring processes and are referred to as "spreading" stages. Stage 9 is a special case in which a gain stage is used to represent the process of sampling array pixels. Finally, Stage 10 is also a special case representing the readout of pixel signals by external electronics. The associated system parameters are defined in Table II.

C. Theoretical evaluation of system performance of imager configurations

A theoretical model, based on cascaded systems formalism,[7,30] was developed for all flat-panel mammographic imager configurations examined in this study. In such a model, an imager configuration is represented as a series of stages. Each stage represents a physical process that governs the transfer of signal and noise information from the input of the stage to the output. Following the formalism described in Ref. 31, the model was constructed to account for parallel stochastic processes associated with the scattering of light photons between the array and the exit surface of the scintillator.[20] Expressions derived from the model were used to quantitatively examine the performance of the imager configurations under various mammographic conditions. In the following sections, the model is described, theoretical expressions for system performance are presented, and methods of obtaining values for parameters required in the calculations are detailed.

1. Cascaded systems model

The signal and noise transfer properties of the imager configurations were examined using the cascaded systems model illustrated in Fig. 3. A number of elementary stages, arranged in series and in parallel, are used to represent the chain of (cascading) processes involved in the formation of x-ray images. Table II lists imaging system parameters and symbols used in the model depicted in Fig. 3.

In the imaging chain, x-ray quanta are incident on the imager (represented by Stage 0), where the mean fluence, $\bar{q}_0$, characterizes the signal and noise of the input quanta. A fraction of the input quanta interact with the scintillator (Stage 1) with a quantum detection efficiency of $\bar{g}_1$. This stage represents a binomial selection process with a gain of $\bar{g}_1$. The x-ray interactions result in the deposition of energy from which light photons are generated. A fraction of these light photons exit from the bottom surface of the fiber optic plate (FOS-HR or FOS-HL) or the Min-R screen (Stage 2). This stage corresponds to a stochastic amplification process in which both a quantum gain, $\bar{g}_2$, and an associated noise (which is quantified in terms of a gain variance, $\sigma^2_{g_2}$, or a Poisson excess, ε_{g_2}) determine the transfer properties of the stage. In the x-ray scintillator, light photons are generated isotropically and undergo multiple scattering before exiting the scintillator (Stage 3). Such optical scattering creates a stochastic blur, which is characterized by the MTF of the stage (T_3), and results in the modulation of the signal and noise information input to the stage.

The surface of the scintillator facing the array is very reflective and the array contains a large number of highly reflective metal lines as well as many layers of different materials, each with a different index of refraction. Therefore, based on a binomial selection process (Stage 4) with a gain of $\bar{\rho}_4$, some of the exiting light photons undergo further scattering between the exit surface of the scintillator and the array (Stage 5)—such multiple scattering is quantified by T_5. The remaining photons are not scattered and are therefore attributed a MTF, T_6, of unity (Stage 6), with a corresponding probability of $\bar{\eta}_4$ (i.e., $\bar{\eta}_4 = 1 - \bar{\rho}_4$). These two parallel processes, Stages 5 and 6, are statistically correlated since they share a common input (Stage 4). Hereafter, Stages 4, 5, and 6 are collectively referred to as the optical interface stage.

Light photons emerging from the scintillator and incident on the photodiode largely pass through the upper layers of the photodiode and interact in its intrinsic a-Si:H layer creating signal charges ($e-h$ pairs) for further readout (Stage 7). This optical coupling of the scintillator to the photodiode is characterized by a probability, $\bar{g}_7$. The finite dimensions of the photodiode determine the photodiode MTF, T_8, and cause a deterministic blur in the signal and noise information (Stage 8) when the light photons are detected. The resulting

TABLE II. Glossary of terms and symbols used in the cascaded systems model depicted in Fig. 3.

Imaging system parameters and miscellaneous symbols	
X	Exposure (mR)
$\Phi(E)$	X-ray spectrum
$\bar{q}_0$	Mean x-ray fluence (x rays/mm^2)
$\bar{g}_i$	Gain (or efficiency) of stage i
ε_{g_i}	Poisson excess associated with a gain stage i
I	Swank factor
T_i	MTF of stage i
S_i	Output noise (NPS) of stage i
S_{add}	Additive noise (NPS)
σ_{add}	Additive noise [e (rms)]
III	Sampling grid represented by a 2-D comb function
(x,y)	Spatial coordinates (mm)
(u,v)	Spatial frequency coordinates (mm^{-1})

signals are sampled by a sampling function representing the two-dimensional array of pixels (Stage 9). Finally, the noise of the electronic acquisition system, σ_{add}, which is statistically independent of other x-ray-quantum-related noise sources, is added to the imaging chain (Stage 10).

2. Cascaded systems expressions for evaluating system performance

Predictions of system performance were made using expressions based on the cascaded systems model described above. The predicted values were compared to empirically determined quantities. The expression for the x-ray sensitivity, Γ, of the imaging pixels is proportional to the product of the gains of the stages:

$$\Gamma = \left(\frac{\bar{q}_0}{X}\right) a_{\mathrm{pd}}^2 \bar{g}_1 \bar{g}_2 (\bar{\rho}_4 + \bar{\eta}_4) \bar{g}_7$$

$$= \left(\frac{\bar{q}_0}{X}\right) a_{\mathrm{pd}}^2 \bar{g}_1 \bar{g}_2 \bar{g}_7 \quad (\text{units:} \ e/\mathrm{mR/pixel}), \tag{3}$$

where X (in units of mR) represents the surface exposure to the imager and a_{pd} (in units of mm) represents the aperture of the photodiode. (a_{pd}^2 corresponds to the optically sensitive area of the photodiode.) The noise power spectra, $S(u,v)$, can be expressed as follows (a derivation is given in Appendix A):

$$S(u,v) = S_8(u,v) {**} \mathrm{III}(u,v) + S_{\mathrm{add}}(u,v)$$

$$= a_{\mathrm{pd}}^4 \bar{q}_0 \bar{g}_1 \bar{g}_2 \bar{g}_7 [1 + \bar{g}_7 (\bar{g}_2 + \varepsilon_{g2}) T_3^2(u,v)$$

$$\times (\bar{\rho}_4 T_5(u,v) + \bar{\eta}_4 T_6(u,v))^2] T_8^2(u,v) {**} \mathrm{III}(u,v)$$

$$+ S_{\mathrm{add}}(u,v) \quad (\text{units:} \ e^2 \, \mathrm{mm}^2). \tag{4a}$$

The cross-spectral noise density, which arises from the correlation of the two parallel processes (represented by Stages 5 and 6), is included in the presampling NPS, $S_8(u,v)$. Furthermore, the process of sampling (Stage 9) is represented by the convolution of $S_8(u,v)$ with the Fourier transform of the sampling grid, which is expressed as

$$\mathrm{III}(u,v) = \sum_{k,l=-\infty}^{\infty} \delta(u - ku_s, v - lv_s). \tag{4b}$$

In this expression, u_s and v_s correspond to the sampling frequency determined by the pixel pitch.

The addition of the NPS associated with electronic acquisition noise, $S_{\mathrm{add}}(u,v)$, yields the total NPS expression given in Eq. (4a). $S_{\mathrm{add}}(u,v)$ was measured in the manner previously described in Sec. II B 3 and served as an empirical input to the NPS model. The product of the calculated sensitivity, Γ, and the exposure used in the determination of the NPS and the DQE, X gives the mean detector signal, $\bar{d}$, and the expressions in Eqs. (3), (4a), and (7) [see Sec. II C 3] can be incorporated into Eq. (2) to arrive at the following expression for the DQE:

$$\mathrm{DQE}(u,v) = \frac{a_{\mathrm{pd}}^4 \bar{q}_0 [\bar{g}_1 \bar{g}_2 \bar{g}_7 T_3(u,v)(\bar{\rho}_4 T_5(u,v) + \bar{\eta}_4 T_6(u,v)) T_8(u,v)]^2}{S(u,v)}. \tag{5}$$

3. Determination of system parameters

For the theoretical performance evaluation, the required system parameters either were deduced from empirical data obtained from the imager configurations or calculated using published results. A summary of the parameter values is given in Table III. To obtain some of these parameters (the scintillator gain, $\bar{g}_2$, and the Poisson excess, ε_{g2}), it was necessary to determine the absorbed energy distribution, AED, for each scintillator and the corresponding pulse height distribution, PHD.[32–35] AED is defined as the distribution of the amount of x-ray energy absorbed following each x-ray interaction, $\mathrm{AED}(E)$. PHD is the probability distribution of the number of optical photons that are generated and emitted from the scintillator per x-ray interaction.

For all calculations of system parameters directly related to the incident x rays, previously reported mammographic spectra[36] were used in order to account for the effects of the energy distribution. The hardening of the x-ray spectra by a

TABLE III. Summary of system parameters used in the model shown in Fig. 3 and their associated values at an x-ray energy of 26 kVp. The system parameter symbols are defined in Table II. The modeled beam corresponds to a Mo/Mo (target/filter) combination with a filtration of a BR12 breast phantom. The thickness of the phantom (4.9 cm) was chosen so that the modeled beam gives a HVL value matching the corresponding measurement (0.059 cm). In all calculations, a nominal value of 2000 e (rms) was assumed for the additive electronic noise, σ_{add}, and the values of $\bar{g}_7$ were reduced by 10% in order to account for the signal loss due to the trapping of charge in the photodiode. The estimates of $\bar{\rho}_4$ were not needed in the calculations and are therefore not shown in this table. (This is discussed further in Sec. II C 3.)

System parameters	Min-R configuration	FOS-HR configuration	FOS-HL configuration
$\bar{q}_0/X$ (x rays/mm^2/mR)	44000	44000	44000
$\bar{g}_1$	0.75	0.86	0.86
$\bar{g}_2$	321	136	312
ε_{g2}	189	2	6
I	0.63	0.98	0.98
$\bar{g}_7$	0.48	0.49	0.49

BR12 phantom and a compression paddle was included in the calculations using the appropriate total mass attenuation data. [The thickness of the BR12 phantom was slightly adjusted so that the calculated half-value layer matches that obtained from measurement (0.059 cm).] The phantom has an elemental composition, and an associated weight fraction (in percent), of H[96], C[70.3], N[1.9], O[17.0], Cl[0.2], Ca[0.9] and a density of 0.98 g/cm^3. The compression paddle was simulated by 3 mm of Plexiglas with a composition of H[8.1], C[60.0], O[32.0] and a density of 1.19 g/cm^3. In the calculation of x-ray fluence per unit exposure ($\bar{q}_0/X$), an appropriate normalization was performed to account for the polyenergetic nature of the incident x rays, as described in Ref. 37.

In order to estimate the quantum detection efficiency ($\bar{g}_1$) and the AED in the scintillator, Monte Carlo calculations under mammographic conditions were performed. This involved the use of an extended version of the EGS4 code[38,39] which implements a general treatment of photoelectric interactions in compounds or mixtures at diagnostic energies. Production, transport, and reabsorption of K fluorescent and L fluorescent x-ray photons were included in the calculations. In addition, the scintillators were modeled using a cylindrical geometry with a 20 cm radius, and a thickness of 93 μm of Gd_2O_2S:Tb for Min-R (corresponding to a surface density of 34 mg/cm^2 and a 50% packing density[40]) and 150 μm of CsI:Tl for FOS-HR and FOS-HL (assuming a 100% packing density). In the simulation for each scintillator, a pencil beam of x rays was incident perpendicular to the center of the end of the cylinder. For each of one million Monte Carlo histories, x-ray interactions were tracked and the amount of deposited energy was tallied. The AED was then calculated by tabulating the occurrence of the energy deposition over all the histories using an energy bin size of 0.5 keV.

The mean scintillator gain ($\bar{g}_2$) was calculated using the expression

$$\bar{g}_2 = \gamma \frac{\bar{E}_{ab}}{\bar{E}_{opt}}, \tag{6}$$

where γ is the screen conversion efficiency[41] which is defined as the efficiency for converting x-ray energy absorbed in a scintillator into light photons which are produced in, and escape from, the scintillator. In addition, $\bar{E}_{ab}$ is the mean absorbed energy, which has been estimated from the calculated AED, and $\bar{E}_{opt}$ is the mean energy per emitted light photon, which can be determined from the emission spectra of each scintillator.[15,42] The value of $\bar{E}_{opt}$ used in the calculations was ~ 2.3 eV for Min-R and ~ 2.2 eV for FOS. The screen conversion efficiency, by virtue of its definition, includes the probability for light photons escaping the scintillator, which is referred to as the escape efficiency. For this study, since the required values of the escape efficiency could not be obtained from the literature, γ was deduced through comparisons of measured sensitivities with values obtained from Eq. (3), with γ treated as a free parameter.

Finally, the value of $\bar{g}_7$ was determined from the emission spectra of the scintillator and the quantum light absorption efficiency of the a-Si:H photodiodes of the Hawkeye array.[12] (Measurements performed outside of the present study indicate that the photodiode efficiency of the Hawkeye array is slightly lower than that observed on earlier prototype arrays. For the Hawkeye array used with a Gd_2O_2S screen, this leads to a value of 0.49 for $\bar{g}_7$, which is lower than that reported for earlier arrays, 0.65.[22]) In order to allow valid comparisons with the radiographic measurements, the value of $\bar{g}_7$ in the corresponding calculations was corrected for the loss of signal due to the trapping of charge in the a-Si:H photodiodes. A signal loss of 10% was assumed for all such calculations, based on the measured trapping properties of the array.

The PHD was determined based upon the AED values obtained from Monte Carlo calculations.[22] In this determination, it was assumed that a single "combined process" could be used to represent energy conversion into light photons as well as transport of these photons in the scintillator. This combined process was assumed to follow Poisson statistics and was modeled by means of a Gaussian distribution. For each energy bin in the AED, a corresponding Gaussian distribution is constructed with both the mean and the variance of the distribution set equal to the mean number of corresponding light photons exiting the scintillator for the energy of the bin. The PHD is then formed by superimposing the Gaussian distributions for all the energy bins and summing these distributions, after normalizing each distribution to the corresponding AED probability.[35]

Moments of the PHD were used to calculate the Swank factor, I,[32] which, in turn, was used to determine the Poisson excess, ε_{g_2}, for each of the Min-R and FOS scintillators.[7] In general, the Swank factor quantifies noise contributions from three major statistical distributions in x-ray imaging:[32] the incident x-ray energy distribution; the absorbed energy distribution (AED); and the optical pulse distribution (OPD) which results from the statistical variation of light photons escaping from the scintillator due to uneven light transport before the escape. In the case of the FOS-HR and FOS-HL scintillators, the contribution of the OPD to the Swank noise is expected to be small due to the assumption that the combined process of energy conversion into light photons and optical transport of those photons within the scintillator follows Poisson statistics. Thus, the calculated Swank noise is largely determined by the AED factor. This observation is consistent with an earlier empirical analysis of Swank noise for columnar CsI scintillators.[43] In the case of the Min-R scintillator, the aforementioned assumption is probably invalid since multiple scattering of light in the powdered phosphor screen exhibits complex light transport properties[44] and consequently contributes much larger noise than would otherwise be expected. Therefore, the value of the Swank noise for the Min-R scintillator was deduced from the measurements of Swank noise for a Lanex Fine screen,[34] which has a similar surface density and material configuration.

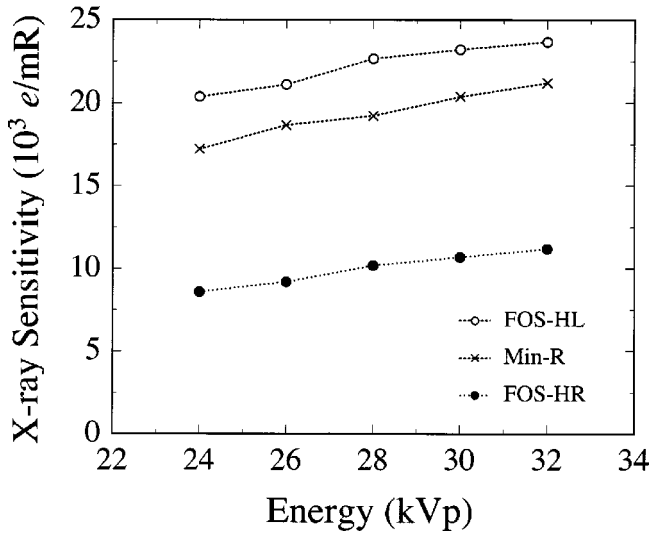The MTF of the entire system, $T_{sys}(u,v)$, is given by an

FIG. 4. Measured radiographic x-ray sensitivities for the Min-R, FOS-HR, and FOS-HL configurations at beam energies ranging from 24 to 32 kVp. Results are plotted in units of the pixel signal per unit exposure to the imager (e/mR).

expression involving all of the MTFs in the present cascaded systems model:

$$T_{\text{sys}}(u,v) = T_3(u,v)[\bar{\rho}_4 T_5(u,v) + \bar{\eta}_4 T_6(u,v)]T_8(u,v)$$

$$\approx T_3(u,v)T_{\text{opt}}(u,v)T_8(u,v), \tag{7}$$

where $T_3(u,v)$ for each scintillator was obtained from published data[15,45] and $T_8(u,v)$ was calculated using the sinc function corresponding to the geometry of the photodiode.[46] In addition, the term $T_{\text{opt}}(u,v)$, representing the overall MTF of the optical interface stage, was deduced from the empirical MTF for the system, assuming that Eq. (7) correctly represents the total system MTF. The individual MTF components were then used in the calculation of the frequency-dependent NPS and DQE.

III. RESULTS

A. X-ray sensitivity

Radiographic x-ray sensitivities were measured for the Min-R, FOS-HR, and FOS-HL imager configurations for x-ray beam energies ranging from 24 to 32 kVp. The results, in units of pixel signal per unit exposure to the imager, are plotted as a function of energy in Fig. 4. The figure shows that x-ray sensitivity generally increases with energy. This is due to the fact that x-ray sensitivity, as defined, is a measure of the energy absorbed in the scintillator per unit energy absorbed in air (i.e., normalized to x-ray exposure). Since the energy absorption coefficient of the scintillator, $(\mu_{\text{ab}}/\rho)_{\text{scint}}$, relative to that of the air, $(\mu_{\text{ab}}/\rho)_{\text{air}}$, increases with x-ray energy,[47] the corresponding x-ray sensitivity is expected to increase, given that other factors are relatively constant over the energy range of interest. The figure also shows that, at all energies, the magnitude of the x-ray sensitivity for the Min-R
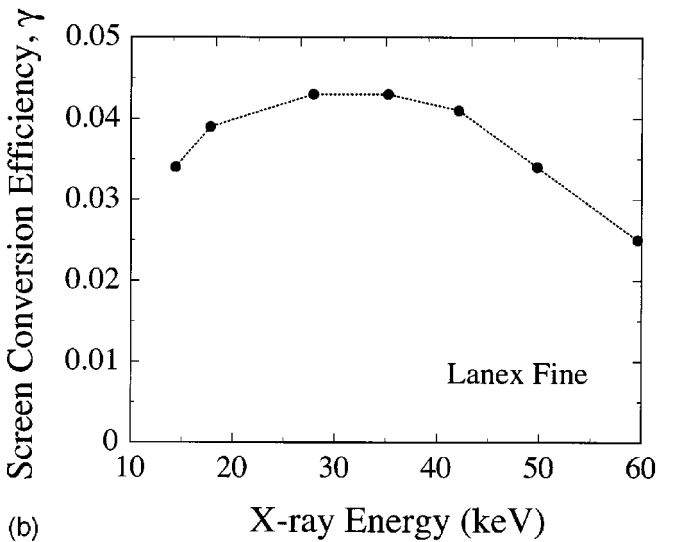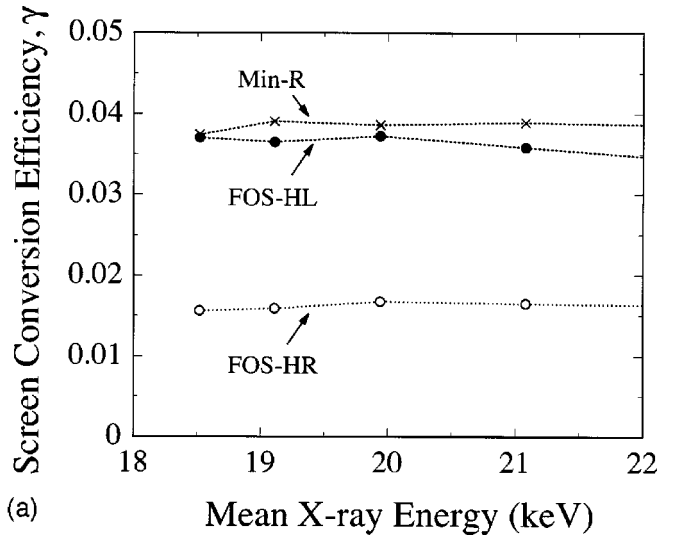

FIG. 5. (a) A plot of the screen conversion efficiency (γ) for the Min-R, FOS-HR, and FOS-HL scintillators. These values were deduced by fitting the expression for sensitivity [given by Eqs. (3) and (6)] to the corresponding measurements plotted in Fig. 4. The other factors in the sensitivity expression were determined through Monte Carlo calculations and measurements. (b) A plot of deduced values of γ for the Lanex Fine scintillator (Ref. 34) which is known to have a surface density and material composition ($\sim$34 mg/cm^2 of Gd$_2$O$_2$S:Tb) similar to that of the Min-R scintillator.

configuration is systematically larger than that for the FOS-HR configuration and smaller than that for the FOS-HL configuration.

From these x-ray sensitivities, values for the screen conversion efficiency of each scintillator, γ, were deduced as described in the previous section. The deduced values of γ are plotted as a function of the mean energy of each mammographic spectrum in Fig. 5(a). These results for γ suggest that the FOS-HR scintillator is less efficient (by over a factor of 2) than the Min-R and FOS-HL scintillators in converting x-ray energy into emitted light photons. The values of γ exhibited by the FOS scintillators account for light attenuation in the 3 mm thick fiber optical plate which is coupled to the CsI:Tl scintillators. The mean transmission efficiency of such
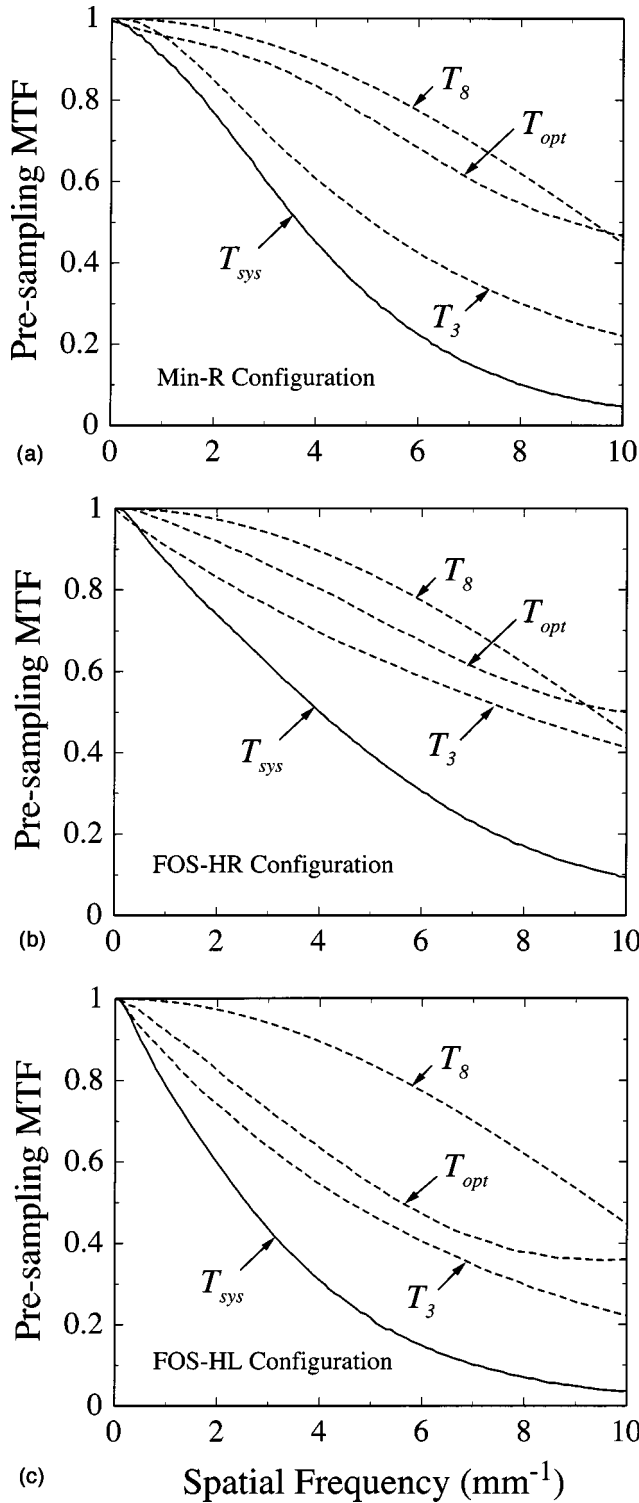
FIG. 6. Plots of the measured system MTF (T_{sys}) and the associated measured and calculated MTF components: the scintillator MTF (T_3); the optical interface MTF (T_{opt}); and the photodiode MTF (T_8). Results are given for (a) the Min-R imager configuration, (b) the FOS-HR imager configuration, and (c) the FOS-HL imager configuration, nearly up to the sampling frequency (~ 10.3 mm^{-1}) of the Hawkeye array.
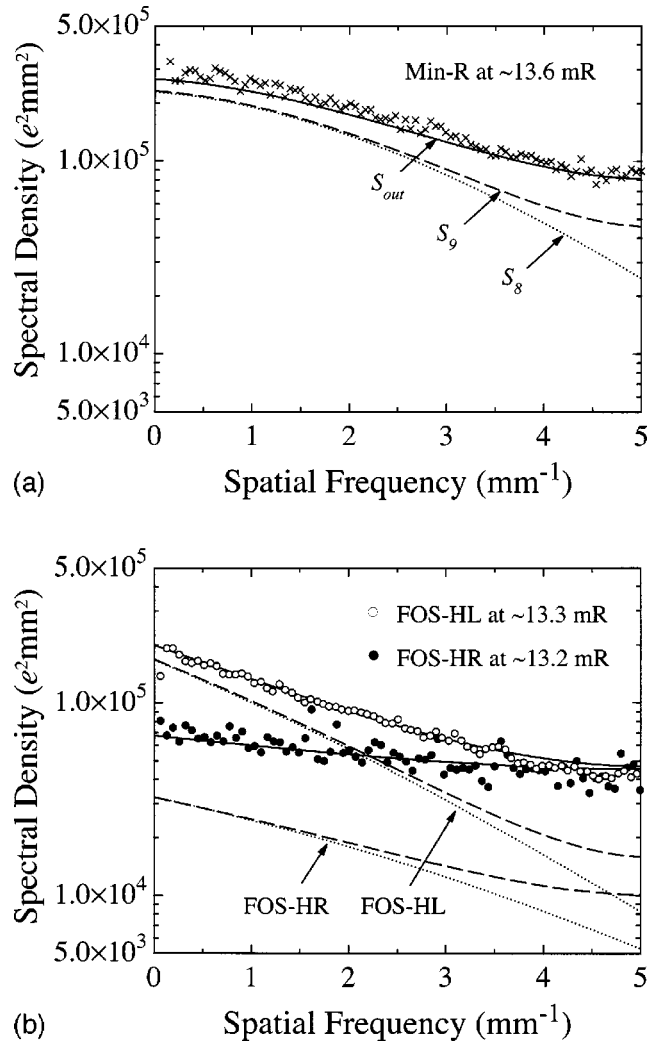

FIG. 7. A plot of the measured (symbols) and calculated (lines) NPS for (a) the Min-R imager configuration and (b) the FOS-HR and FOS-HL configurations, at a mammographic exposure of ~ 13 mR. $S_8(u)$, $S_9(u)$, and $S_{out}(u)$ correspond to the calculated NPS at Stage 8 (presampling stage, dotted line), 9 (sampling stage, dashed line), and 10 (total output stage, solid line), respectively. $S_9(u)$ was obtained by introducing the effect of noise power aliasing to the $S_8(u)$ calculation. $S_{out}(u)$ was calculated by adding the dark NPS, $S_{add}(u)$, to the $S_9(u)$ calculation.

an optical plate has been estimated to be only $\sim 60\%$.[15] Values of γ obtained for another Gd_2O_2S:Tb screen, which have been obtained from an analysis of data reported in Ref. 34, are shown in Fig. 5(b). A comparison of the screen converter efficiencies for the Min-R and Lanex Fine screens in Figs. 5(a) and 5(b), respectively, indicates that the values are very similar, as would be expected given their similar composition and thickness. This similarity supports the assumption that the method used to deduce values of γ may be equally well applied to the two FOS scintillators.

B. Modulation transfer function (MTF)

In the cascaded systems model used in this study, the MTF of the x-ray scintillator, T_3, is modulated by the optical interface MTF, T_{opt}, and the photodiode MTF, T_8. The product of the three MTFs gives the MTF for the entire imaging system, T_{sys}. In Figs. 6(a), 6(b), and 6(c), measured values for T_{sys}, as well as the associated three MTF components, are shown for the Min-R, FOS-HR, and FOS-HL configurations, respectively. The results are plotted as a function of

spatial frequency, approximately up to the sampling frequency (10.3 mm^{-1}) of the imager. The figures show that the Min-R and the FOS-HR scintillators exhibit relatively high MTF (T_3) for all frequencies, indicating that these scintillators have been optimized for spatial resolution. As described in Sec. II C 3, values for T_{opt} were deduced from the measurements of T_{sys} for each configuration. A comparison of T_{opt} for the Min-R and the FOS-HR configurations shows that these optical interface MTFs are similar in magnitude and shape. Moreover, the measured (presampling) T_{sys} values indicate that both imager configurations exhibit considerable MTF well beyond the Nyquist frequency (5.2 mm^{-1}). Compared to T_{sys} of the FOS-HR configuration, the Min-R T_{sys} is slightly higher up to ~2.7 mm^{-1} and becomes lower thereafter. The FOS-HL configuration generally exhibits lower T_{sys} than the other two configurations at all frequencies. This is also evident in the results for T_3 and T_{opt}. The low values of T_{opt} for the FOS-HL configuration may be indicative of a lower degree of optical coupling between the array surface and the scintillator. At the Nyquist frequency, the Min-R, FOS-HR, and FOS-HL configurations exhibit T_{sys} values of ~0.30, 0.38, and 0.18, respectively.

C. Noise power spectra (NPS)

Measurements and theoretical calculations of NPS(u) were performed for the Min-R, FOS-HR, and FOS-HL imager configurations. Figures 7(a) and 7(b) show results at an incident exposure of ~13 mR for the Min-R and FOS configurations, respectively, under irradiation conditions commonly used with screen-film systems. These spectral density results have been plotted in absolute units (i.e., e^2 mm^2), as opposed to the more common convention of reporting NPS normalized to the mean signal level, in order to preserve the correspondence between the magnitude of each NPS result and the magnitude of the system gain for the corresponding imager configuration. In order to quantitatively illustrate the effects of noise power aliasing and additive noise for each AMFPI configuration, theoretical calculations of the NPS at three different stages in the calculation are plotted: (a) prior to the inclusion of noise power aliasing and additive noise [presampling stage, $S_8(u)$]; (b) with aliasing but prior to the inclusion of additive noise [sampling stage, $S_9(u)$]; and (c) the total calculation [final output stage, $S_{out}(u)$].

In these figures, good agreement is generally observed between the full calculation and the measurements for all imager configurations, although the theory slightly underestimates the empirical NPS(u) for the Min-R configuration at low and medium frequencies. In the case of the FOS-HL configuration, the theory is slightly higher than the corresponding measurements at high frequencies. All three configurations exhibit high presampling NPS, $S_8(u)$, at frequencies above the Nyquist frequency (~5.2 mm^{-1}–beyond what is shown in the figure), consistent with the high (presampling) MTF of the system at these frequencies. Consequently, this high level of spectral density, after sampling, results in an increase in noise below the Nyquist frequency
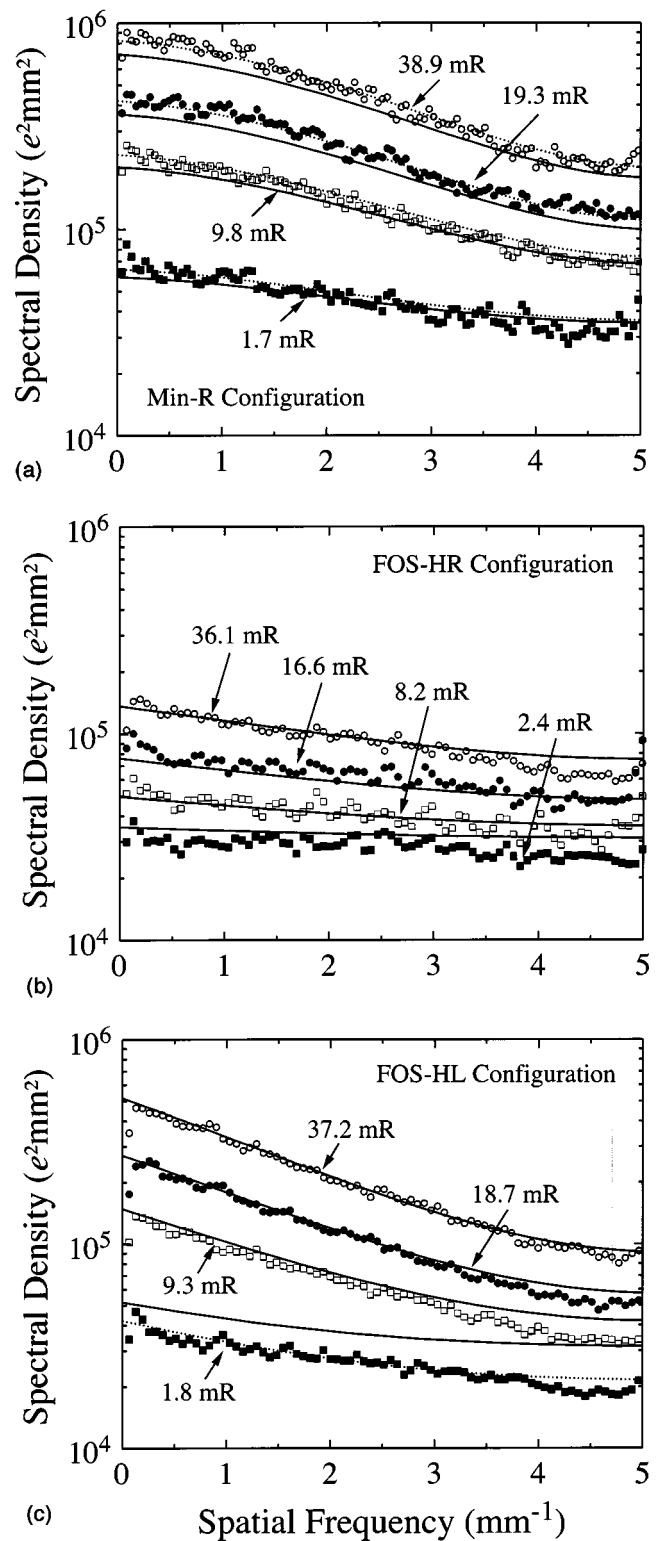

FIG. 8. A plot of the measured (symbols) and calculated (lines) NPS, $S_{out}(u)$, for (a) the Min-R, (b) the FOS-HR, and (c) the FOS-HL imager configurations. Results are presented for a variety of exposures using a frame time optimized for each exposure level. In (a), the solid lines correspond to a Swank factor of 0.63 (taken from that for Lanex Fine) while the dotted lines correspond to a reduced Swank factor of 0.53. For the 1.8 mR results in (c), additional calculations were performed using a $S_{add}(u)$ value (~2.0×10^4 e^2 mm^2) lower than the measured one (~2.9×10^4 e^2 mm^2). These calculations are shown by a dotted line. (See the main text for further details.)

due to noise power aliasing. The generally good agreement between the empirical NPS(u) and the full calculation, $S_{out}(u)$, is a clear indication that the model is accurately accounting for the effect of such aliasing.

The generally lower NPS exhibited by the FOS-HR configuration compared to those of the Min-R and FOS-HL configurations, evident in Figs. 7(a) and 7(b), is due to the lower system gain of the FOS-HR configuration. In addition, the calculations before $[S_9(u)]$ and after $[S_{out}(u)]$ the inclusion of the additive noise, $S_{add}(u)$, indicate that the relative contribution of $S_{add}(u)$ to $S_{out}(u)$ is much greater for the FOS-HR configuration than for the Min-R and FOS-HL configurations—again due to the lower system gain of the FOS-HR configuration. For the frame time corresponding to the irradiations used in these measurements, the empirically determined dark NPS, $S_{add}(u)$, was found to be $\sim 3.5 \times 10^4$ e^2 mm^2 and was independent of spatial frequency. At an incident exposure of ~ 13 mR, the relative size of $S_{add}(u)$ to $S_{out}(u)$ is $\sim 52\%$, $\sim 13\%$, and $\sim 16\%$ near zero frequency for the FOS-HR, Min-R, and FOS-HL configurations, respectively.

In Figs. 8(a), 8(b), and 8(c), the dependence of the NPS upon exposure is shown for the Min-R, FOS-HR, and FOS-HL configurations, respectively. For each configuration, NPS(u) was determined at four exposure levels (1.7, 9.8, 19.3, and 38.9 mR for the Min-R configuration, 2.4, 8.2, 16.6, and 36.1 mR for the FOS-HR configuration, and 1.8, 9.3, 18.7, and 37.2 mR for the FOS-HL configuration). Other than at the lowest exposure where additive noise contributes significantly to the noise power, the measured NPS is found to increase in an approximately linear manner with increasing exposure, consistent with theoretical expectations. Although the magnitude of the measured dark NPS, $S_{add}(u)$, was essentially identical for all configurations, $S_{add}(u)$ did vary as a function of the frame time used to accommodate each exposure. Accordingly, values of $S_{add}(u)$ ranging from $\sim 2.9 \times 10^4$ to $\sim 4.7 \times 10^4$ e^2 mm^2 were used as empirical inputs for the theoretical calculations shown in Fig. 8.

In the case of the Min-R configuration, the cascaded systems model accurately predicts the shape of the measured NPS. However, the model systematically underestimates the magnitude of the measured NPS at all but the lowest exposure, 1.7 mR. A plausible cause for this discrepancy is an underestimation of the Swank noise (i.e., an overestimation of the Swank factor) used in the theoretical calculations. In these calculations, due to a lack of published data, the Swank noise for the Min-R scintillator was based on empirical data obtained from the Lanex Fine screen which has a similar surface density and material configuration. However, despite these similarities, the design of the Min-R scintillator may well be configured differently in order to optimize light transport to achieve better MTF performance. Therefore, the Min-R scintillator may have a Swank noise characteristic significantly different from that for the Fine screen. Interestingly, the replacement of the Lanex Fine Swank factor of 0.63 by an arbitrarily chosen value of 0.53 in the calculation results in excellent agreement with the measurements at all exposures—supporting the idea that the value of 0.63 is in-
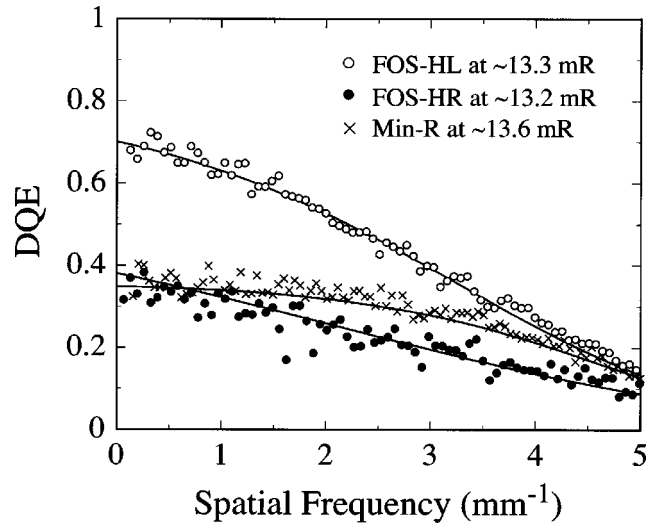

FIG. 9. A plot of the measured (discrete symbols) and calculated (lines) DQE for the Min-R, FOS-HR, and FOS-HL imager configurations at a nominal mammographic exposure of ~ 13 mR. These data correspond to the NPS results shown in Fig. 7. DQE(u) is plotted up to the Nyquist frequency of the Hawkeye array. For the DQE calculations for the Min-R configuration in Figs. 9 and 10, an adjusted value of 0.53 was assumed for the Swank factor.

deed an overestimate for the Min-R Swank factor.

Compared to the Min-R and FOS-HL configurations at similar exposures, the FOS-HR configuration exhibits lower NPS(u) at all frequencies due to the effect of lower system gain, as previously noted for the data in Fig. 7(b). In addition, the relative contribution of the additive noise to the total output NPS is much greater for the FOS-HR configuration than for the Min-R and FOS-HL configurations. As a result, the general shape of the FOS-HR total NPS is more influenced by the white noise behavior of the dark NPS. Figure 8(b) shows that there is fair agreement between the FOS-HR measurements and the calculations for each exposure. Slight disagreements observed at 2.4 and 16.6 mR are possibly due to the fluctuation of external, environmental noise contributions during the accompanying dark NPS measurements.

In the case of the FOS-HL configuration [Fig. 8(c)], the absolute magnitude of the total NPS is found to be larger than that for the FOS-HR configuration (due to the effect of higher system gain) but slightly smaller than that for the Min-R configuration (due to the effect of lower Swank noise). In addition, the NPS of the FOS-HL configuration is found to decrease significantly with increasing spatial frequency—consistent with the shape of the MTF. Once again, good agreement is found between the measurements and the corresponding calculations for all exposures except for 1.8 mR where theory overestimates the corresponding measurement by an estimated amount of $\sim 9.9 \times 10^3$ e^2 mm^2 at all frequencies. Since the discrepancy is frequency-independent, it is likely to have been caused by an overestimation of $S_{add}(u)$ during the dark NPS measurements.
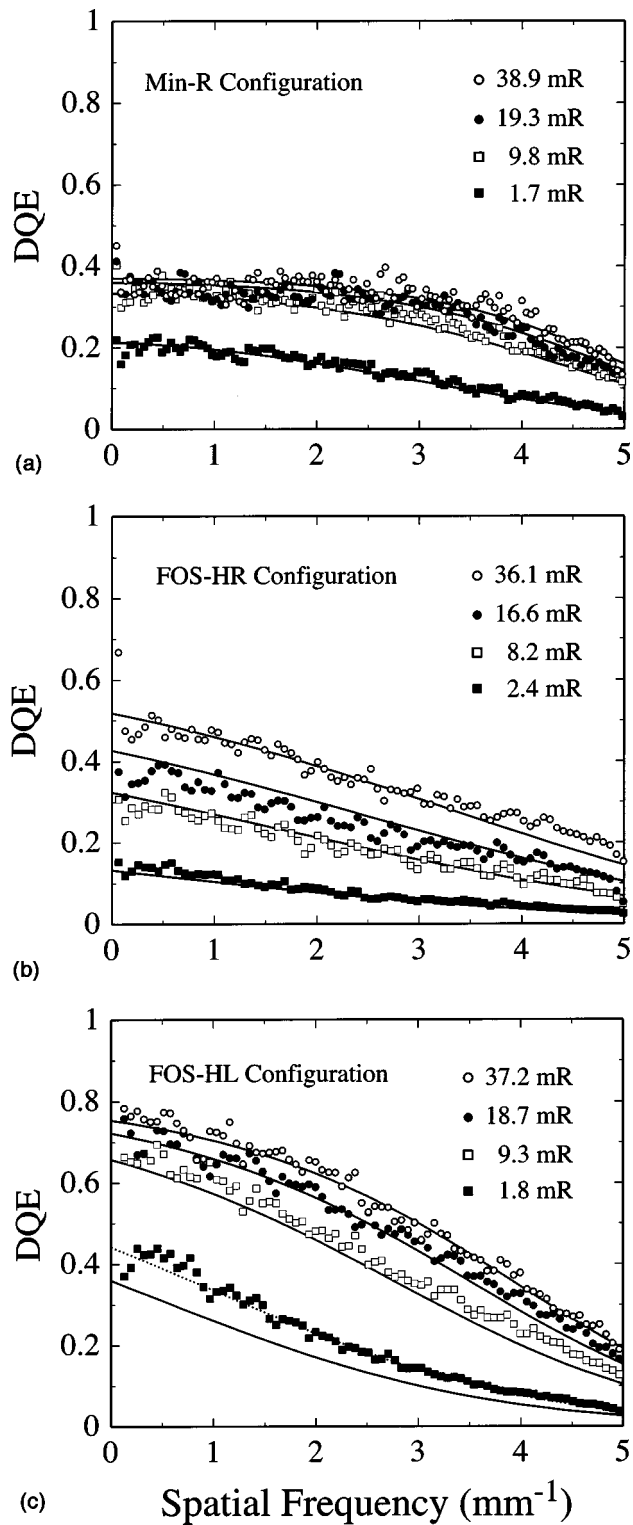
FIG. 10. A plot of the measured (symbols) and calculated (lines) DQE for (a) the Min-R, (b) the FOS-HR, and (c) the FOS-HL imager configurations. The data correspond to the NPS results of Fig. 8. In (c), the dotted line corresponds to DQE calculations using an adjusted $S_{add}(u)$ value of $\sim 2.0 \times 10^4$ e^2 mm^2.

D. Detective quantum efficiency (DQE)

Detective quantum efficiency for the Min-R, FOS-HR, and FOS-HL configurations was determined from the mea-

surements of mean detector signal, MTF, and NPS using Eq. (2). This determination also involved the use of a calculated x-ray fluence of $\sim 44\,000$ photons/mm^2/mR corresponding to the 26 kVp mammographic beam described in Sec. II B. For each set of measurement conditions, theoretical calculations were performed using Eq. (5) and compared to the corresponding empirical results. Note that, for reasons described in the previous section, an adjusted value of 0.53 was used for the Swank factor for the Min-R calculations.

In Fig. 9, DQE(u) is plotted for the Min-R, FOS-HR, and FOS-HL configurations at exposures of 13.6, 13.2, and 13.3 mR, respectively. The Min-R and FOS-HR configurations exhibit DQE values as high as ~ 0.4 near zero frequency and thereafter show either a gradual decrease (for Min-R) or a more rapid decrease (for FOS-HR). At all frequencies above ~ 0.5 mm^{-1}, the DQE is found to be higher for the Min-R configuration than for the FOS-HR configuration. In the case of the FOS-HL configuration, the DQE starts much higher, ~ 0.7 near zero frequency, and decreases rapidly with increasing frequency down to ~ 0.1 at ~ 5.0 mm^{-1}. The data clearly demonstrate that, even though the FOS-HL configuration offers physical properties (i.e., quantum detection efficiency and Swank noise) similar to those of the FOS-HR configuration and lower resolution than either the FOS-HR or Min-R configurations, it nonetheless outperforms the FOS-HR and Min-R configurations at all frequencies below the Nyquist frequency. The theoretical calculations show good agreement with the measured DQE for each imager configuration.

In Figs. 10(a), 10(b), and 10(c), further determinations of DQE(u) based on measurements and using Eq. (2), along with the corresponding calculations using Eq. (5), are plotted for the Min-R, FOS-HR, and FOS-HL configurations, respectively. Results are shown for the same detector exposures used in the NPS studies reported in Sec. III C. Good agreement is generally observed between the measurements and the calculations at each exposure. Figure 10(a) shows that the DQE performance of the Min-R configuration is low (~ 0.2 near zero frequency) at ~ 1.7 mR and improves with increasing exposure until converging to a value of ~ 0.37. Theoretical analysis indicates that, for exposures above ~ 10 mR, the effect of the additive noise (from the electronics) upon the Min-R DQE performance is minimal and that the DQE performance is limited primarily by the Swank noise of the Min-R scintillator. Measurements indicate that the DQE values are indeed lower than the estimated Min-R Swank factor (~ 0.53). However, in the case of the FOS-HR configuration, the DQE performance is strongly affected by the presence of the additive noise due to the low gain of the system. As a result, as shown in Fig. 10(b), the DQE values continue to rise with increasing exposure with convergence presumably occurring at exposure levels beyond those examined in this study. Such strong dependence on x-ray exposure is reduced when a higher gain x-ray converter, such as the FOS-HL scintillator, is employed in the imager configuration. Figure 10(c) shows that the FOS-HL configuration exhibits DQE performance that improves with increasing exposure at a much faster rate than the FOS-HR configuration—

resulting in DQE values significantly higher (greater than ~0.65 near zero frequency, even at an exposure as low as ~9 mR) than those for the FOS-HR configuration.

IV. SUMMARY AND CONCLUSIONS

In this paper, active matrix flat-panel imagers configured for the application of mammography were evaluated in terms of x-ray sensitivity and frequency-dependent observer independent performance variables including MTF, NPS, and DQE. Measurements were performed for three indirect detection imager configurations incorporating a 97 μm pitch flat-panel array coupled to three different x-ray converters, a Gd_2O_2S-based mammographic screen (Min-R) and two structured CsI:Tl scintillators (FOS-HR and FOS-HL). X-ray sensitivity was measured at various energies ranging from 24 to 32 kVp, MTF was measured at 26 kVp, and NPS and DQE were determined for a variety of mammographic exposures at 26 kVp. The measured NPS and DQE were also compared to theoretical calculations based on a cascaded systems model. This model incorporates parallel cascades of stochastic processes accounting for multiple scattering of light photons between the opposing surfaces of the flat-panel array and the scintillator.

The results of the sensitivity measurements show that the Min-R and FOS-HL configurations exhibit higher signal output for a given incident exposure (i.e., higher x-ray sensitivity) than the FOS-HR configuration by a factor of over two (Fig. 4). The theoretical analysis (Fig. 5) indicates that both the Min-R and FOS-HL scintillators are more efficient in the generation and emission of light photons than the FOS-HR scintillator—the deduced screen conversion efficiency being ~3.9 and 3.7% for the Min-R and FOS-HL, respectively, as compared to only ~1.6% for the FOS-HR. The measurements of system MTF (Fig. 6) show that the Min-R and FOS-HR configurations exhibit higher MTF than the FOS-HL configuration. For the FOS converters, this is a clear demonstration of the tradeoff between spatial resolution and light output. In addition, all three configurations show high MTF at frequencies above the Nyquist limit (~5.2 mm^{-1}) which induces noise power aliasing in the measurements of NPS. In general, the spatial resolution of the scintillator (i.e., the scintillator MTF) is found to be a dominant component of the system MTF, although the contribution of the optical interface MTF is also significant in the case of the FOS-HL.

Consistent with their high system MTF, the imager configurations exhibit relatively high NPS at higher frequencies up to the Nyquist limit (Figs. 7 and 8). The absolute magnitude of the output noise power increases in an approximately linear fashion with increasing x-ray exposure. Due to their high system gain, the Min-R and FOS-HL configurations exhibit noise performance limited primarily by the x-ray quantum noise—which is a highly desirable situation. However, for the FOS-HR configuration, the relative contribution of the electronics noise remains significant across the nominal mammographic exposures. As a result, the FOS-HR configuration exhibits DQE performance considerably more dependent upon x-ray exposure than the Min-R and FOS-HL configurations—a situation which is not so desirable.

The determination of DQE from measurements (Figs. 9 and 10) shows that the highest level of DQE performance offered by the Min-R imager configuration (~37%) is superior to that of conventional film-screen systems using the same, or very similar, x-ray converters (~30%).[48,49] However, such film-screen systems are capable of providing information at considerably higher spatial frequencies than the Min-R configuration by virtue of the inherently high spatial resolution of film compared to the relatively low Nyquist frequency of the Hawkeye array. Theoretical analysis indicates that, despite the quantum detection efficiency, $\bar{g}_1$, being as high as ~0.75, the upper limit of the Min-R DQE performance is strongly limited by the large Swank noise of the Min-R screen. The FOS configurations, which incorporate 150 μm thick CsI:Tl scintillators, provide high values for $\bar{g}_1$ (~0.86) and I (~0.98 at 26 kVp) which offer the potential of achieving high DQE performance.

Measurements indeed show that the FOS-HL configuration (the high system gain configuration) exhibits excellent DQE values across a wide range of mammographic exposures, particularly above ~10 mR. However, the FOS-HR configuration (the high resolution configuration) exhibits DQE values only comparable to, or less than, those of the Min-R configuration. In particular, the FOS-HR configuration exhibits DQE performance which is strongly dependent on x-ray exposure (due to the low gain of the system), thereby further diminishing the benefits of having high spatial resolution. For the FOS converters, these results illustrate the, perhaps, nonobvious effects on DQE when tradeoffs are made between spatial resolution and light output.

Overall, good agreement between the cascaded systems calculations and the measurements for NPS and DQE was observed. Particularly at high spatial frequencies, the model demonstrates improved accuracy in predicting NPS and DQE when the parallel branch concept is added to our previous linear model.[46] It should also be emphasized that the results of the cascaded systems calculations strongly depended on the input values for model parameters. Therefore, for any such theoretical study, extensive efforts should be made to obtain accurate values for all model parameters.

It is interesting to note that the present study was initially designed to evaluate only the two high-resolution converters, Min-R and FOS-HR. However, the cascaded systems analysis of the results from these converters strongly suggested that significant improvement in DQE performance could be attained through a sacrifice of some spatial resolution for increases in system gain—a prediction that was shown to be accurate when results from the FOS-HL converter were obtained. This is an example of how cascaded systems modeling can be used to identify factors limiting DQE system performance and to examine trade offs between factors toward the goal of maximizing performance.

The general advantages offered by active matrix flat-panel imaging technology (including real-time digital readout and compactness) make the idea of very high resolution AMFPIs (e.g., down to pixel pitches of ~50 μm) highly attractive.

However, maintaining a degree of DQE performance at least comparable or, preferably, superior to that of present mammographic film-screen systems is almost certainly a prerequisite for the clinical acceptance of such hypothetical devices. For both direct and indirect detection, previous studies strongly suggest that achieving high system gain, while maintaining relatively low additive noise levels, is essential for achieving high DQE for sub-100 μm pitch devices.[50] While it is unclear if present AMFPI devices using direct detection (with a-Se) and indirect detection (with discrete photodiodes) can provide a level of gain sufficient to ensure high DQE performance down to 50 μm pixel pitch, improvements such as the introduction of high gain photoconductors (PbI$_2$ and HgI$_2$)[51,52] and continuous photodiodes[53,54] will significantly contribute toward achieving the necessary gain enhancements. Furthermore, the present studies demonstrate that, through optimization guided by accurate modeling (for example, involving the careful tradeoff of spatial resolution for an increased signal), the potential performance of AMFPI designs can be maximized.

ACKNOWLEDGMENTS

APPENDIX: NOISE POWER SPECTRUM

The following derivation of noise power spectrum (NPS) is based on a cascaded systems model developed for an indirect detection, mammographic flat-panel imager. This model (illustrated in Fig. 3) is an extended version of a general form shown in Ref. 46. Specifically, the present model is identical to the general model except for the addition of stages (i.e., Stages 4, 5, and 6) which account for the light scattering process between the exit surface of the converter and the top surface of the array.

Using the noise transfer equations, Eqs. (2a), (2b), and (2c), in Ref. 46, the NPS at the output of each stage is calculated as follows:

$$S_1(u,v) = \bar{g}_1^2 S_0(u,v) + \bar{q}_0 \bar{g}_1 (1 - \bar{g}_1) = \bar{q}_0 \bar{g}_1, \tag{A1}$$

$$S_2(u,v) = \bar{g}_2^2 S_1(u,v) + \sigma_{g_2}^2 \bar{q}_0 \bar{g}_1$$
$$= \bar{q}_0 \bar{g}_1 \bar{g}_2^2 + \bar{g}_2(\varepsilon_{g_2} + 1)\bar{q}_0 \bar{g}_1$$
$$= \bar{q}_0 \bar{g}_1 \bar{g}_2 (1 + \bar{g}_2 + \varepsilon_{g_2}), \tag{A2}$$

$$S_3(u,v) = [S_2(u,v) - \bar{q}_0 \bar{g}_1 \bar{g}_2]T_3^2(u,v) + \bar{q}_0 \bar{g}_1 \bar{g}_2$$
$$= [\bar{q}_0 \bar{g}_1 \bar{g}_2(1 + \bar{g}_2 + \varepsilon_{g_2}) - \bar{q}_0 \bar{g}_1 \bar{g}_2]T_3^2(u,v)$$
$$+ \bar{q}_0 \bar{g}_1 \bar{g}_2$$
$$= \bar{q}_0 \bar{g}_1 \bar{g}_2 [1 + (\bar{g}_2 + \varepsilon_{g_2})T_3^2(u,v)]. \tag{A3}$$

At Stage 4, some photons are randomly selected (based on a

binomial probability, $\bar{\rho}_4$) and propagate through Stage 5 (path A). The remaining photons travel through Stage 6 with a probability $\bar{\eta}_4 = 1 - \bar{\rho}_4$ (path B). Stages 5 and 6 are statistically correlated since they both share a common input, Stage 4. Hence, the output NPS of Stages 4, 5, and 6, or collectively called $S_{\text{opt}}(u,v)$, can be determined by the sum of the output NPS from both paths and their cross-spectral noise density terms:

$$S_{\text{opt}}(u,v) = S_5(u,v) + S_6(u,v) + S_{AB}(u,v) + S_{BA}(u,v). \tag{A4}$$

Transferring $S_3(u,v)$ through a binomial gain and a stochastic spreading stage, the NPS of Stages 5 and 6 are obtained as

$$S_5(u,v) = \bar{q}_0 \bar{g}_1 \bar{g}_2 \bar{\rho}_4 [1 + \bar{\rho}_4(\bar{g}_2 + \varepsilon_{g_2})T_3^2(u,v)T_5^2(u,v)], \tag{A5}$$

$$S_6(u,v) = \bar{q}_0 \bar{g}_1 \bar{g}_2 \bar{\eta}_4 [1 + \bar{\eta}_4(\bar{g}_2 + \varepsilon_{g_2})T_3^2(u,v)T_6^2(u,v)]. \tag{A6}$$

Using Eq. (103) in Ref. 31, the cross-spectral density term can be expressed as

$$S_{AB}(u,v) = \bar{\rho}(1 - \bar{\rho})\bar{k}^A \bar{k}^B T^A(u,v)T^B(u,v)$$
$$\times [S_3(u,v) - \bar{q}_0 \bar{g}_1 \bar{g}_2]$$
$$= \bar{\rho}_4(1 - \bar{\rho}_4)T_5(u,v)T_6(u,v)$$
$$\times [S_3(u,v) - \bar{q}_0 \bar{g}_1 \bar{g}_2]$$
$$= \bar{q}_0 \bar{g}_1 \bar{g}_2 \bar{\rho}_4 \bar{\eta}_4 (\bar{g}_2 + \varepsilon_{g_2})$$
$$\times T_3^2(u,v)T_5(u,v)T_6(u,v), \tag{A7}$$

where $\bar{k}^A$ and $\bar{k}^B$ (T^A and T^B) represent a mean gain (MTF) along path A and B, respectively. In the same manner, $S_{BA}(u,v)$ is obtained as

$$S_{BA}(u,v) = \bar{q}_0 \bar{g}_1 \bar{g}_2 \bar{\rho}_4 \bar{\eta}_4 (\bar{g}_2 + \varepsilon_{g_2})$$
$$\times T_3^2(u,v)T_5(u,v)T_6(u,v). \tag{A8}$$

Substituting (A5)–(A8) to (A4), $S_{\text{opt}}(u,v)$ is then calculated as follows:

$$S_{\text{opt}}(u,v) = S_5(u,v) + S_6(u,v) + S_{AB}(u,v) + S_{BA}(u,v)$$
$$= \bar{q}_0 \bar{g}_1 \bar{g}_2 [(\bar{\rho}_4 + \bar{\eta}_4) + (\bar{g}_2 + \varepsilon_{g_2})$$
$$\times (\bar{\rho}_4^2 T_3^2(u,v)T_5^2(u,v) + \bar{\eta}_4^2 T_3^2(u,v)T_6^2(u,v)$$
$$+ 2\bar{\rho}_4 \bar{\eta}_4 T_3^2(u,v)T_5(u,v)T_6(u,v))]$$
$$= \bar{q}_0 \bar{g}_1 \bar{g}_2 [1 + (\bar{g}_2 + \varepsilon_{g_2})T_3^2(u,v)$$
$$\times (\bar{\rho}_4 T_5(u,v) + \bar{\eta}_4 T_6(u,v))^2]. \tag{A9}$$

In Stage 7, light photons are coupled to the photodiode:

$$S_7(u,v) = \bar{g}_7^2 S_{opt}(u,v) + \sigma_{g_7}^2 \bar{q}_0 \bar{g}_1 \bar{g}_2$$

$$= \bar{q}_0 \bar{g}_1 \bar{g}_2 \bar{g}_7 [1 + \bar{g}_7(\bar{g}_2 + \varepsilon_{g_2})$$

$$\times T_3^2(u,v)(\bar{\rho}_4 T_5(u,v) + \bar{\eta}_4 T_6(u,v))^2]. \quad (A10)$$

After integrating light photons to the photodiode aperture in Stage 8, we have

$$S_8(u,v) = a_{pd}^4 S_7(u,v) T_8^2(u,v)$$

$$= a_{pd}^4 \bar{q}_0 \bar{g}_1 \bar{g}_2 \bar{g}_7 [1 + \bar{g}_7(\bar{g}_2 + \varepsilon_{g_2}) T_3^2(u,v)$$

$$\times (\bar{\rho}_4 T_5(u,v) + \bar{\eta}_4 T_6(u,v))^2] T_8^2(u,v). \quad (A11)$$

The process of spatial sampling is given by a convolution of the presampling noise, $S_8(u,v)$, with the Fourier transform of the sampling grid, $III(u,v)$:

$$S_9(u,v) = S_8(u,v) ** III(u,v)$$

$$= a_{pd}^4 \bar{q}_0 \bar{g}_1 \bar{g}_2 \bar{g}_7 [1 + \bar{g}_7(\bar{g}_2 + \varepsilon_{g_2}) T_3^2(u,v)(\bar{\rho}_4 T_5(u,v)$$

$$+ \bar{\eta}_4 T_6(u,v))^2] T_8^2(u,v) ** III(u,v), \quad (A12)$$

where $III(u,v)$ is represented by a 2-D comb function, $\Sigma_{k,l=-\infty}^{\infty} \delta(u - ku_s, v - lv_s)$ with sampling frequencies u_s and v_s.

Finally, at Stage 10, the NPS associated with additive electronic noise, $S_{add}(u,v)$, is added to the output of Stage 9:

$$S_{10}(u,v) = S_9(u,v) + S_{add}(u,v)$$

$$= a_{pd}^4 \bar{q}_0 \bar{g}_1 \bar{g}_2 \bar{g}_7 [1 + \bar{g}_7(\bar{g}_2 + \varepsilon_{g_2}) T_3^2(u,v)$$

$$\times (\bar{\rho}_4 T_5(u,v) + \bar{\eta}_4 T_6(u,v))^2]$$

$$\times T_8^2(u,v) ** III(u,v) + S_{add}(u,v). \quad (A13)$$

a)Corresponding author: Kyung-Wook Jee, Department of Radiation Oncology, University of Michigan Medical Center, 1500 E. Medical Center Drive, Ann Arbor, Michigan 48109. Phone: 734-936-4309; fax: 734-936-7859; electronic mail: wook@umich.edu

[1] M. L. Giger and K. Doi, "Investigation of basic imaging properties in digital radiography, Modulation transfer function," Med. Phys. **11**, 287–295 (1984).

[2] M. L. Giger, K. Doi, and C. E. Metz, "Investigation of basic imaging properties in digital radiography. 2. noise Wiener spectrum," Med. Phys. **11**, 797–805 (1984).

[3] C. E. Metz, R. F. Wagner, K. Doi, D. G. Brown, R. M. Nishikawa, and K. J. Myers, "Toward consensus on quantitative assessment of medical imaging systems," Med. Phys. **22**, 1057–1061 (1995).

[4] S. Vedantham, A. Karellas, S. Suryanarayanan, D. Albagli, S. Han, E. J. Tkaczyk, C. E. Landberg, P. R. Granfors, I. Levis, C. J. D'Orsi, and R. E. Hendrick, "Full breast digital mammography with an amorphous silicon-based flat panel detector: Physical characteristics of a clinical prototype," Med. Phys. **27**, 558–567 (2000).

[5] B. Polischuk, S. Savard, V. Loustaneau, M. Hansroul, S. Cadieux, and A. Vaque, "Se-based flat-panel detector for screening mammography," Proc. SPIE **4320**, 582–589 (2001).

[6] J. G. Yorker, L. S. Jeromin, D. Lee, E. F. Palecki, K. P. Golden, and Z. Jing, "Characterization of a full field digital mammography detector based on direct x-ray conversion in selenium," Proc. SPIE **4682**, 21–29 (2002).

[7] I. Cunningham, M. Westmore, and A. Fenster, "A spatial-frequency dependent quantum accounting diagram and detective quantum efficiency model of signal and noise propagation in cascaded imaging systems," Med. Phys. **21**, 417–427 (1994).

[8] J. H. Siewerdsen, L. E. Antonuk, Y. El-Mohri, J. Yorkston, W. Huang, and I. A. Cunningham, "Signal, noise power spectrum, and detective quantum efficiency of indirect-detection flat-panel imagers for diagnostic radiology," Med. Phys. **25**, 614–628 (1998).

[9] L. E. Antonuk, K.-W. Jee, Y. El-Mohri, C. Nassif, M. Maolinbay, X. Rong, and Q. A. Zhao, "Strategies to improve signal and noise performance of active matrix, flat-panel imagers for diagnostic x-ray applications," Med. Phys. **27**, 289–306 (2000).

[10] L. E. Antonuk, Y. El-Mohri, A. Hall, K.-W. Jee, M. Maolinbay, S. C. Nassif, X. Rong, J. H. Siewerdsen, Q. Zhao, and R. L. Weisfield, "A large-area, 97 μm pitch, indirect-detection, active matrix flat-panel imager," Proc. SPIE **3336**, 2–13 (1998).

[11] R. A. Street, S. Nelson, L. E. Antonuk, and V. Perez Mendez, "Amorphous silicon sensor arrays for radiation imaging," Mater. Res. Soc. Symp. Proc. **192**, 441–452 (1990).

[12] L. E. Antonuk, Y. El-Mohri, J. H. Siewerdsen, J. Yorkston, W. Huang, V. E. Scarpine, and R. A. Street, "Empirical investigation of the signal performance of a high-resolution, indirect detection, active matrix flat panel imager (AMFPI) for fluoroscopic and radiographic operation," Med. Phys. **24**, 51–70 (1997).

[13] L. E. Antonuk, Y. El-Mohri, W. Huang, K.-W. Jee, J. H. Siewerdsen, M. Maolinbay, V. E. Scarpine, H. Sandler, and J. Yorkston, "Initial performance evaluation of an indirect-detection, active matrix flat-panel imager (AMFPI) prototype for megavoltage imaging," Int. J. Radiat. Oncol., Biol., Phys. **42**, 437–454 (1998).

[14] L. E. Antonuk, J. Yorkston, W. Huang, J. Boudry, E. J. Morton, M. Longo, and R. A. Street, "Factors affecting image quality for megavoltage and diagnostic x-ray a-Si:H imaging arrays," Mater. Res. Soc. Symp. Proc. **258**, 1069–1074 (1992).

[15] Technical document, "FOS (fiber optic plate scintillator) for digital x-ray imaging," Hamamatsu Photonics K. K., TMCP9003E01, 1998.

[16] W. Huang, L. E. Antonuk, J. Berry, M. Maolinbay, C. Martelli, P. Mody, S. Nassif, and M. Yeakey, "An asynchronous, pipelined, electronic acquisition system for Active Matrix Flat-Panel Imagers (AMFPIs)," Nucl. Instrum. Methods Phys. Res. A **431**, 273–284 (1999).

[17] R. J. Yarema, T. Zimmerman, J. Sarage, L. E. Antonuk, J. Berry, W. Huang, and M. Maolinbay, "A programmable, low noise, multichannel asic for readout of pixelated amorphous silicon arrays," Nucl. Instrum. Methods Phys. Res. A **439**, 413–417 (2000).

[18] *ACR Mammography Quality Control Manual*, American College of Radiology, 1999.

[19] H. Fujita, D. Tsai, T. Itoh, K. Doi, J. Morishita, K. Ueda, and A. Ohtsuka, "A simple method for determining the modulation transfer function in digital radiography," IEEE Trans. Med. Imaging **11**, 34–39 (1992).

[20] J. Yorkston, L. E. Antonuk, N. Seraji, W. Huang, J. H. Siewerdsen, and Y. El-Mohri, "MTF measurements with high resolution a-Si:H imaging arrays," Proc. SPIE **2432**, 260–269 (1995).

[21] L. E. Antonuk, J. Boudry, W. Huang, D. L. McShan, E. J. Morton, J. Yorkston, M. J. Longo, and R. A. Street, "Demonstration of megavoltage and diagnostic x-ray imaging with hydrogenated amorphous silicon arrays," Med. Phys. **19**, 1455–1466 (1992).

[22] Y. El-Mohri, K.-W. Jee, L. E. Antonuk, M. Maolinbay, and Q. Zhao, "Determination of the detective quantum efficiency of a prototype, megavoltage indirect detection, active matrix flat-panel imager," Med. Phys. **28**, 2538–2550 (2001).

[23] A. D. Maidment and M. J. Yaffe, "Analysis of the spatial-frequency-dependent DQE of optically coupled digital mammography detectors," Med. Phys. **21**, 721–729 (1994).

[24] J. C. Dainty and R. Shaw, *Image Science: Principles, Analysis and Evaluation of Photographic-Type Imaging Processes* (Academic, London, 1974).

[25] M. L. Giger, K. Doi, and C. E. Metz, "Investigation of basic imaging properties in digital radiography. 2. noise Wiener spectrum," Med. Phys. **11**, 797–805 (1984).

[26] Y. El-Mohri, L. E. Antonuk, Q. Zhao, M. Maolinbay, X. Rong, K.-W. Jee, S. Nassif, and C. Cionca, "A quantitative investigation of additive noise reduction for active matrix flat-panel imagers using compensation lines," Med. Phys. **27**, 1855–1864 (2000).

[27] M. B. Williams, P. A. Mangiafico, and P. U. Simoni, "Noise power spectra of images form digital mammography," Med. Phys. **26**, 1279–1293 (1999).

[28] J. T. Dobbins, D. L. Ergun, L. Rutz, D. A. Hinshaw, H. Blume, and D. C.

Clark, "DQE(f) of four generations of computed radiography acquisition devices," Med. Phys. **22**, 1581–1593 (1995).

[29] X. Wu, G. T. Barns, and D. M. Tucker, "Spectral dependence of glandular tissue dose in screen-film mammography," Radiology **179**, 143–148 (1991).

[30] I. A. Cunningham and R. Shaw, "Signal-to-noise optimization of medical imaging systems," J. Opt. Soc. Am. A **16**, 621–632 (1999).

[31] J. Yao and I. A. Cunningham, "Parallel cascades: New ways to describe noise transfer in medical imaging systems," Med. Phys. **28**, 2020–2038 (2001).

[32] R. K. Swank, "Absorption and noise in x-ray phosphors," J. Appl. Phys. **44**, 4199–4203 (1973).

[33] H.-P. Chan and K. Doi, "Studies of x-ray energy absorption and quantum noise properties of x-ray screens by use of Monte Carlo simulation," Med. Phys. **11**, 37–46 (1984).

[34] D. P. Trauernicht and R. Van Metter, "The measurement of conversion noise in x-ray intensifying screens," Proc. SPIE **914**, 100–116 (1988).

[35] R. Fahrig, J. A. Rowlands, and M. J. Yaffe, "X-ray imaging with amorphous selenium: Detective quantum efficiency of photoconductive receptors for digital mammography," Med. Phys. **22**, 153–160 (1995).

[36] J. M. Boone, T. R. Fewell, and R. J. Jennings, "Molybdenum, rhodium, and tungsten anode spectral models using interpolating polynomials with application to mammography," Med. Phys. **24**, 1863–1874 (1997).

[37] J. M. Boone, "Spectral modeling and compilation of quantum fluence in radiography and mammography," Proc. SPIE **3336**, 592–601 (1998).

[38] H. Hirayama, Y. Namito, and S. Ban, "Implementation of a general treatment of photoelectric-related phenomena for compounds or mixtures in EGS4," KEK Internal 2000-3, May 2000.

[39] Y. Namito and H. Hirayama, "LSCAT: Low-Energy Photon-Scattering Expansion for the EGS4 code (Inclusion of Electron Impact Ionization)," KEK Internal 2000-4, May 2000.

[40] R. M. Nishkawa and M. J. Yaffe, "Signal-to-noise properties of mammographic film-screen systems," Med. Phys. **12**, 32–39 (1985).

[41] R. J. Pizzutiello and J. E. Cullinan, *Introduction to Medical Radiographic Imaging* (Eastman Kodak Company, Rochester, NY, 1993).

[42] G. Zweig and D. A. Zweig, "Radioluminescent imaging: factors affecting total light output," Proc. SPIE **419**, 297–301 (1979).

[43] J. A. Rowlands and K. W. Taylor, "Absorption and noise in cesium iodide x-ray image intensifiers," Med. Phys. **10**, 786–795 (1983).

[44] M. Drangova and J. A. Rowlands, "Optical factors affecting the detective quantum efficiency of radiological screens," Med. Phys. **13**, 150–157 (1986).

[45] P. C. Bunch, "Objective imaging characteristics of mammographic screen-film systems," Proc. SPIE **2708**, 241–271 (1996).

[46] J. H. Siewerdsen, L. E. Antonuk, Y. El-Mohri, J. Yorkston, W. Huang, J. M. Boudry, and I. A. Cunningham, "Empirical and theoretical investigation of the noise performance of indirect detection, active matrix flat-panel imager (AMFPIs) or diagnostic radiology," Med. Phys. **24**, 71–89 (1997).

[47] H. E. Johns and J. R. Cunningham, *The Physics of Radiology* (Thomas, Springfield, 1983).

[48] R. Nishikawa and M. Yaffe, "Signal-to-noise property of mammographic film-screen systems," Med. Phys. **12**, 32–39 (1985).

[49] P. C. Bunch, K. E. Huff, and R. Van Matter, "Analysis of the detective quantum efficiency of a radiographic screen-film combinations," J. Opt. Soc. Am. A **4**, 902–909 (1987).

[50] K.-W. Jee, L. E. Antonuk, Y. El-Mohri, C. Cionca, M. Maolinbay, S. Nassif, and Q. Zhao, "Theoretical investigation of advanced design active matrix flat-panel imagers for mammography," Proc. SPIE **3977**, 250–256 (2000).

[51] R. A. Street *et al.*, "High resolution, direct detection x-ray imagers," Proc. SPIE **3977**, 418–428 (2000).

[52] H. Hermon *et al.*, "Deposition of thick films of polycrystalline mercuric iodide x-ray detectors," Proc. SPIE **4320**, 133–139 (2001).

[53] J. T. Rahn, F. Lemmi, R. L. Weisfield, R. Lujan, P. Mei, J. Lu, J. Ho, S. E. Ready, R. B. Apte, P. Nylen, J. Boyce, and R. A. Street, "High resolution, high fill factor a-Si:H sensor arrays for medical imaging," Proc. SPIE **3659**, 510–517 (1999).

[54] Y. El-Mohri, L. E. Antonuk, K.-W. Jee, Y. Kang, Y. Li, A. Sawant, Z. Su, Y. Wang, J. Yamamoto, and Q. Zhao, "Evaluation of novel direct and indirect detection active matrix, flat-panel imagers (AMFPIs) for mammography," Proc. SPIE **5030**, 168–180 (2003).

[55] M. Maolinbay, Y. El-Mohri, L. E. Antonuk, K.-W. Jee, S. Nassif, X. Rong, and Q. Zhao, "Additive noise properties of active matrix flat-panel imagers," Med. Phys. **27**, 1841 (2000).